Cohesin depleted cells pass through mitosis and reconstitute a functional nuclear architecture

Marion Cremer[1,*,§], Katharina Brandstetter[2,*], Andreas Maiser[2], Suhas S P Rao[3,4],

Volker Schmid[5], Namita Mitra[3], Stefania Mamberti[6], Kyle-N Klein[7], David M Gilbert[7],

Heinrich Leonhardt[2], Maria Cristina Cardoso[6], Erez Lieberman Aiden[3,8,9,10],

Hartmann Harz[2,§], Thomas Cremer[1,§]

1. Anthropology and Human Genomics, Department Biology II, Ludwig-Maximilians-Universität München, Germany

2. Human Biology & BioImaging, Center for Molecular Biosystems, Department Biology II, Ludwig-Maximilians-Universität München, Germany

3. Center for Genome Architecture, Department of Molecular and Human Genetics, Baylor College of Medicine, Houston, Texas, United States of America

4. Department of Structural Biology, Stanford University School of Medicine, California, United States of America

5. BioImaging Group, Department of Statistics, Ludwig-Maximilians-Universität München, Germany

6. Cell Biology and Epigenetics, Department of Biology, Technische Universität Darmstadt, Germany

7. Department of Biological Science, Florida State University, Tallahassee, Florida, United States of America

8. Center for Theoretical Biological Physics, Rice University, Houston, Texas, United States of America

9. Broad Institute of the Massachusetts Institute of Technology and Harvard University, Cambridge, Massachusetts, United States of America

10. Departments of Computer Science and Computational and Applied Mathematics, Rice University, Houston, Texas, United States of America

*equal contribution, § corresponding authors

43 **Abstract**

44 The human genome forms thousands of "contact domains", which are intervals of enhanced

45 contact frequency. Some, called "loop domains" are thought to form by cohesin-mediated loop

46 extrusion. Others, called "compartmental domains", form due to the segregation of active and

47 inactive chromatin into A and B compartments. Recently, Hi-C studies revealed that the

48 depletion of cohesin leads to the disappearance of all loop domains within a few hours, but

49 strengthens compartment structure. Here, we combine live cell microscopy, super-resolution

50 microscopy, Hi-C, and studies of replication timing to examine the longer-term consequences

51 of cohesin degradation in HCT-116 human colorectal carcinoma cells, tracking cells for up to

52 30 hours. Surprisingly, cohesin depleted cells proceed through an aberrant mitosis, yielding a

53 single postmitotic cell with a multilobulated nucleus. Hi-C reveals the continued disappearance

54 of loop domains, whereas A and B compartments are maintained. In line with Hi-C, microscopic

55 observations demonstrate the reconstitution of chromosome territories and chromatin

56 domains. An interchromatin channel system (IC) expands between chromatin domain clusters

57 and carries splicing speckles. The IC is lined by active chromatin enriched for RNA Pol II and

58 depleted in H3K27me3. Moreover, the cells exhibit typical early-, mid-, and late- DNA

59 replication timing patterns. Our observations indicate that the functional nuclear

60 compartmentalization can be maintained in cohesin depleted pre- and postmitotic cells.

61 However, we find that replication foci – sites of active DNA synthesis – become physically

62 larger consistent with a model where cohesin dependent loop extrusion tends to compact

63 intervals of replicating chromatin, whereas their genomic boundaries are associated with

64 compartmentalization, and do not change.

65

66 **Abbreviations**

67 3D FISH = 3D fluorescence in situ hybridization

68 3D SIM = 3D structured illumination microscopy

69 AID = auxin inducible degron

70 ANC / INC = active / inactive nuclear compartment

71 CT = chromosome territory

72 CD(C) = chromatin domain (cluster)

73 CTCF = CCCTC binding factor

74 DAPI = 4',6-diamidino-2-phenylindole

75 EdU = 5-Ethynyl-2'-deoxyuridine

76 Hi-C = chromosome conformation capturing combined with deep sequencing

77 IC = interchromatin compartment

78 MLN = multilobulated nucleus

79 NC = nucleosome cluster

80 PBS = phosphate buffered saline

81 PBST = phosphate buffered saline with 0.02% Tween

82 PR = perichromatin region

83 RD = replication domain

84 RL = replication labeling

85 TAD = topologically associating domain

86

Introduction

Cohesin, a ring-like protein complex with its major subunits RAD21, SMC1 and SMC3 is involved in numerous nuclear processes, such as in double strand break repair and gene regulation, by exerting its key function of tethering distant genomic loci [1-7]. In addition, cohesin entraps sister chromatids to ensure faithful chromosome segregation during mitosis (reviewed in [1]).

In recent years cohesin's ability as shaper of chromatin loops in the sub-Mb range anchored at CTCF/cohesin binding sites [8, 9] has moved into the spotlight of research. Hi-C studies have indicated that these loops, which manifest as bright peaks in contact frequency in a Hi-C map, demarcate contact domains [10, 11]. They manifest as squares of enhanced contact frequency in a Hi-C map and correspond to self-interacting genomic intervals between 50kb and 1Mb where DNA sequences physically interact with each other more frequently compared to sequences outside a given domain [12, 13]. Loop domains thus comprise a structural unit of chromatin organization [14, 15].

Studies on the impact of cohesin in nuclear functions have become highly facilitated by an approach, which triggers a rapid and selective proteolysis of RAD21 by integrating an auxin-inducible degron (AID) system and its fusion to both endogenous RAD21 alleles into a given cell line [16] (for review see [17]). Addition of auxin results in RAD21 proteolysis with the concomitant disintegration of cohesin from chromatin [18].

Using this system in the colon cancer derived HCT116-RAD21-mAC cell line, we recently demonstrated the rapid disappearance of loop domains in Hi-C contact matrices averaged over large cell populations [18]. Compartments, manifesting when chromatin intervals with common histone signatures co-localize [13], were retained and even strengthened, leading to the presence of compartment domains and even compartment loops (but no loop domains) in the treated cells [18]. Other studies, using different cell types and approaches for cohesin elimination yielded similar results [19-21], (reviewed in [22]).

Here, we study the longer-term consequences of cohesin depletion and its effects on the higher order nuclear architecture via a combination of super-resolution and live cell microscopy, as well as Hi-C and Repli-Seq. We found that cohesin depleted interphase cells

4

116   proceed through a greatly prolonged mitosis resulting in a single cell with one multilobulated

117   nucleus (MLN) after chromatid segregation. With Hi-C we confirm both the continued

118   disappearance of loop domains and the maintenance of A and B compartments in MLN. With

119   super-resolved microscopy we demonstrate that nuclei of pre- and postmitotic cohesin

120   depleted cells maintain principal structural features of the ANC-INC model (reviewed in [23-

121   25]). According to this model, which has been supported by electron microscopy and 3D super-

122   resolution fluorescence microscopic studies from various species and cell types, the global

123   nuclear landscape is shaped by chromosome territories (CTs) built up from chromatin domains

124   (CDs) and chromatin domain clusters (CDCs). CDCs show a multilayered shell-like

125   organization with increasing chromatin compaction levels from the periphery toward the interior

126   CDC core. An interconnected system of interchromatin channels, called the interchromatin

127   compartment (IC), pervades the spaces between CDCs. The IC carries splicing speckles and

128   nuclear bodies within IC-lacunas and plays a central role in the formation of various nuclear

129   machineries. IC-channels penetrate the layer of heterochromatin beneath the nuclear

130   envelope and form direct contacts with nuclear pore complexes. The IC is lined by CDs with

131   less compacted chromatin, first described in electron microscopic studies as the perichromatin

132   region (for review see [26]). The PR serves as the preferential nuclear subcompartment for

133   transcription and co-transcriptional splicing. The IC and PR form the active nuclear

134   compartment (ANC), whereas CDs with a more compact, 'closed' chromatin configuration are

135   located further away from the IC and comprise the INC.

136   We also examined replication timing, which has been linked to domain structure [27].

137   Strikingly, the absence of cohesin did not lead to major changes in replication timing or in the

138   genomic extent of replication domains (RDs), indicating that the two structures form by

139   independent mechanisms. Instead, we find that the boundaries of RDs closely match those of

140   the A and B compartments both before and after cohesin degradation. This matches the Repli-

141   Seq findings reported in [28] and is consistent with the observation of [29]. Taken together, our

142   findings indicate that replication domains correspond with compartment domains, but not with

143   loop domains. However, we find that the physical size of replication foci is smaller, suggesting

144   that cohesin-depending extrusion may play a role in the physical compaction of replicating

5

145   chromatin.

146

147   **Results**

148   **Validation of auxin induced proteolysis of the cohesin subunit RAD21**

149   All experiments of this study were performed with the human colon cancer derived cell line

150   HCT116-RAD21-mAC [16], where an auxin-inducible degron (AID) is fused to both

151   endogenous RAD21 alleles and to a fluorescent reporter (see Suppl_Fig.1). The complete loss

152   of RAD21-mClover fluorescence was seen in live cell observations ~1:30h after incubation in

153   500 µM auxin (Suppl_Fig.2A). Degradation of RAD21 was confirmed by negative

154   immunostaining with a RAD21 antibody, while epitopes of cohesin subunits SMC1 and SMC3

155   remained intact under auxin shown by persisting positive immunodetection with respective

156   antibodies (Suppl_Fig.2B). Notably, a small fraction of cells in our cultures (~2-4%) escaped

157   auxin induced RAD21 degradation. In order to exclude non-responsive cells from further

158   analyses of the impact of cohesin depletion, RAD21-mClover fluorescence was routinely

159   recorded in all experiments with auxin treated cell populations except for 3D-FISH experiments

160   since DNA heat denaturation destroys the reporter fluorescence [30].

161

162   **Cohesin depletion leads to delayed mitosis and final transition into a single postmitotic**

163   **cell with a multilobulated nucleus (MLN)**

164   Using time lapse imaging over 21h at Δt=15min, we compared in parallel entrance into mitosis,

165   mitotic progression and exit in untreated controls and in cohesin depleted HCT116-RAD21-

166   mAC cells, where auxin was added just before starting life cell observations. In control cells

167   (Fig. 1A) ~80% of all recorded mitoses (n=45) passed mitosis within <1h and formed two

168   inconspicuous daughter nuclei. A second mitosis observed for individual nuclei ~20h after the

169   first division demonstrates their capacity to divide again under the given observation

170   conditions. Notably, about 20% of mitoses recorded in untreated control cells revealed

171   prolonged mitoses of >2h followed by transition into an abnormal cell nucleus, a feature which

172   is not unusual in tumor cell lines (reviewed in [31]). Mitotic entrance of auxin treated cells

6

173   (n=32) did not show any conspicuous differences to controls (Fig.1B). However, their passage

174   through mitosis was consistently delayed up to 14h (median 4.5h). This prolonged mitotic stage

175   raised the mitotic index in cohesin depleted cell cultures fixed after 6h in auxin to almost 30%

176   versus ~4% in control cultures (Suppl_Fig.3). The delayed mitotic passage was associated

177   with the formation of abnormal multipolar mitotic figures persisting over several hours. Fig. 1C

178   depicts a typical telophase stage of ~30 min with two apparent daughter nuclei preceding the

179   formation of a single MLN. Despite their seemingly separation, these daughter nuclei, however,

180   were presumably still connected by filaments (see below) and did not enter into cytokinesis.

181   Instead, all cohesin depleted cells that were followed through an entire mitosis (n=19) resulted

182   in a single MLN (Fig.1B-C). As a consequence, in cell cultures fixed 28-30h after cohesin

183   depletion, MLN accumulated up to ~60% versus ~2% in control cultures (Suppl_Fig.3). MLN

184   were noted in cell cultures kept up to 50h where a considerable fraction of apoptotic cell nuclei

185   indicated their decline (data not shown).
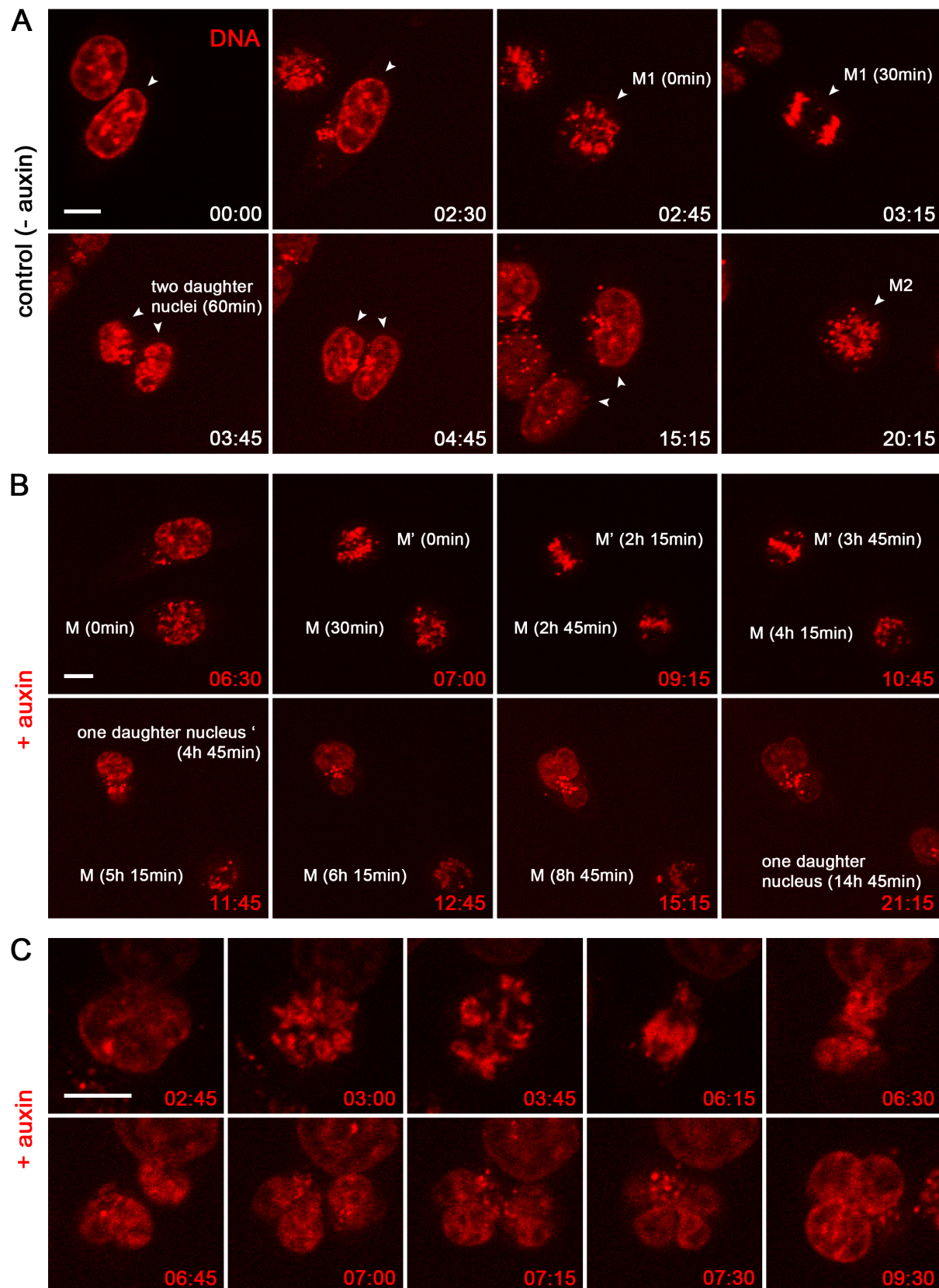
Fig. 1: Live cell microscopy demonstrating highly prolonged abnormal mitosis and subsequent formation of one multilobulated nucleus (MLN) in cohesin depleted cells

(A) Selected points from time lapse imaging ($\Sigma t=21h$, $\Delta t=15min$) of untreated control cells (DNA stained with SiR-DNA, red) with accomplishment of mitosis (M1) within 1h (time 02:45 – 03:45) and

191 subsequent formation of two daughter nuclei. A second mitosis (M2) of one daughter nucleus is

192 shown at time 20:15. **(B)** Selected time lapse images of nuclei after cohesin degradation conducted

193 in parallel to control cells demonstrate a prolonged mitotic stage. Mitosis (M) emerges at time 6:30

194 after auxin treatment, transition into one abnormal multilobulated daughter nucleus (MLN) is seen

195 14:45h later (time 21:15). Mitosis (M') emerges 7h after auxin treatment (time 07:00), transition into

196 an MLN is seen 4:45h later (time 11:45). **(C)** Time lapse imaging from the same series at a higher

197 zoom shows the formation of an aberrant mitosis apparently reaching telophase at time 6:30. 15

198 min later two seemingly separated daughter nuclei, presumably connected by filaments, become

199 fused into one MLN at time 7:15. Scale bar: 10 µm

200

201 **Global features of higher order chromatin organization persist after cohesin depletion**

202 **and are re-established in MLN after mitosis despite the loss of loop domains**

203

204 *Maintenance and re-formation of chromosome territories (CTs)*

205 Maintenance of a territorial organization of interphase chromosomes in cohesin depleted cell

206 cultures was tested by chromosome painting of CTs 4, 12 and 19 (Fig. 2). In line with the near-

207 diploid karyotype of HCT116 cells [32, 33], two homologous territories of each painted

208 chromosome were detected in interphase nuclei of both control (Fig. 2A) and cohesin depleted

209 cells fixed after 6h auxin treatment (Fig. 2B). Segregation of chromatids in cohesin depleted

210 cells was noted in anaphase (Fig. 2C, mid). Accordingly, a substantial fraction of postmitotic

211 MLN revealed four painted territories often located in different lobuli (Fig. 2D). Unexpectedly,

212 chromosome painting, however, detected also MLN with more than four variably sized painted

213 segments for a given painted chromosome (Fig. 2E and Suppl_Fig. 4). Arguably, chromatids

214 were torn apart by mechanic forces during an aberrant anaphase and/or during lobe formation.

215 This disruption was possibly enhanced by a higher level of relaxation / decondensation in

216 cohesin depleted chromatin (see below).

9
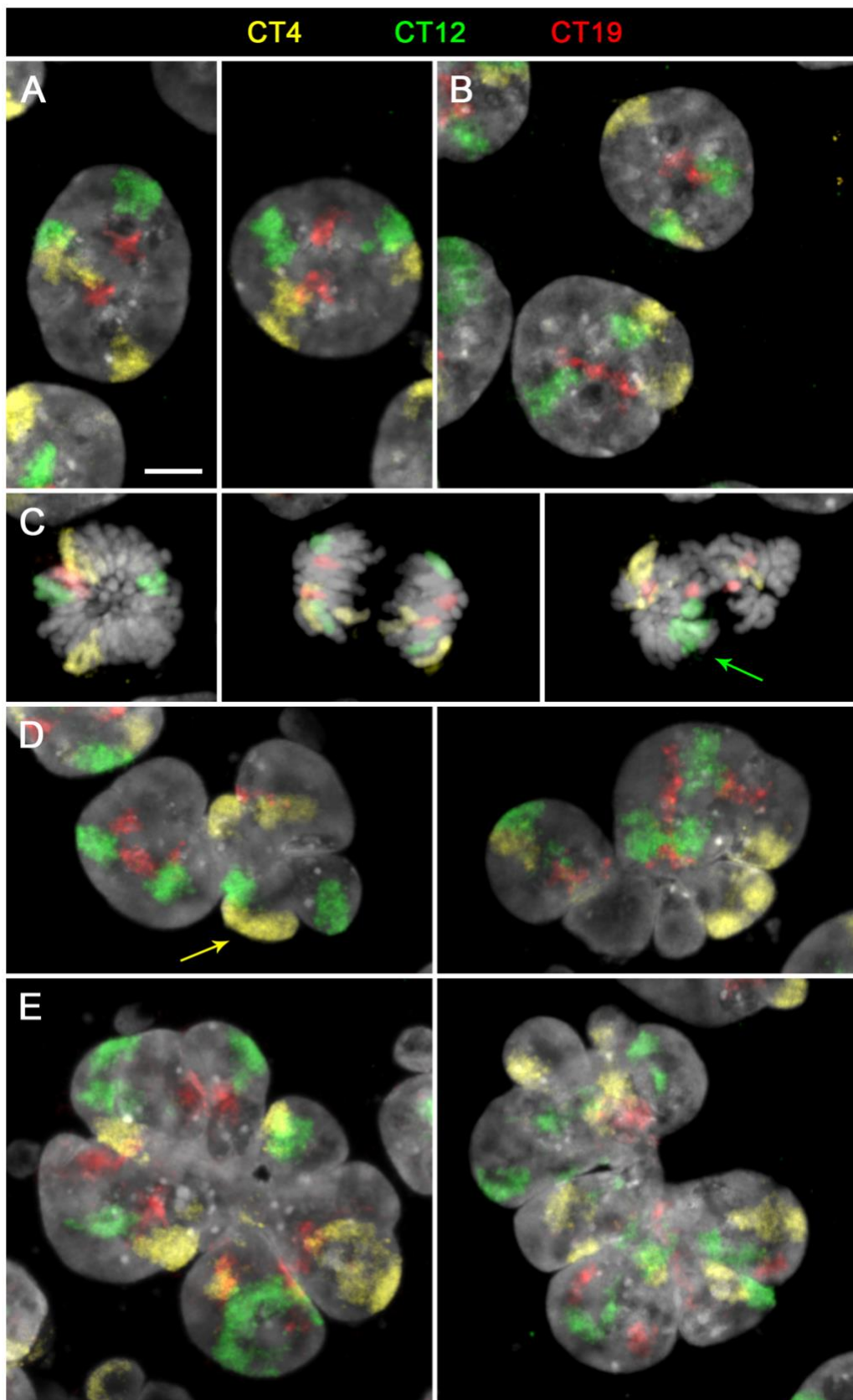
**Fig. 2: Maintenance of chromosome territories (CTs) in cohesin depleted nuclei and their re-establishment after mitosis**

(A-E) Z-projections of entire DAPI stained nuclei (gray) with painted territories of chromosomes 4 (yellow), 12 (green) and 19 (red) acquired by confocal fluorescence microscopy. **(A)** Control nuclei

222 and **(B)** cohesin depleted premitotic nuclei with normal phenotypes after 6h in auxin show two

223 inconspicuous copies for each CT. **(C)** Mitoses from 6h auxin treated cultures with two coherent

224 chromosomes in an (early) metaphase plate *(left),* segregated chromatids in anaphase *(mid)* and

225 missegregation of chromosome 12 (arrow) in an abnormal mitotic figure *(right).* **(D)** Postmitotic

226 multilobulated nuclei (MLN) with four copies for each CT. Arrow marks two CTs 4 that cannot be

227 distinguished in the z-projection. **(E)** MLN with >4 painted regions for each CT (compare also

228 Suppl_Fig. 4). Scale bar: 5 µm

229

230 *Maintenance of co-aligned functionally interacting active and inactive nuclear compartments*

231 *(ANC-INC) in nuclei of cohesin depleted pre- and postmitotic cells*

232 3D structured illumination microscopy (3D-SIM) revealed similar chromatin compaction

233 patterns both in DAPI stained control and cohesin depleted nuclei, including postmitotic MLN.

234 This and other findings described below provide evidence for major structural and functional

235 features of the ANC-INC model (Fig. 3 and 4, and introduction). For a quantitative analysis of

236 nuclear serial sections, DAPI fluorescence was divided into seven intensity classes with equal

237 intensity variance (color code in Fig.3). This representation of nuclear landscapes as color heat

238 maps with increasing DNA densities (Fig 3 A-C) served as proxy for classes with increasing

239 chromatin compaction [34]. Class 1 (lowest DNA density) represents the interchromatin

240 compartment (IC), classes 2 (and 3) comprise low compaction CDs lining the IC. At the nuclear

241 periphery IC-channels expand between lamina associated domains toward nuclear pores (Fig.

242 3D-F). The quantitative assessment of voxels attributed to the seven DAPI intensity classes

243 showed a slight shift towards less compacted chromatin (classes 1 and 2) in cohesin depleted

244 nuclei compared to controls (Fig. 3G), in line with a slight increase of nuclear volumes after 6h

245 cohesin depletion. The ~2-fold increased nuclear volume in MLN (30h auxin) reflects the

246 double amount of DNA in these postmitotic cells. (Fig. 3H).

11
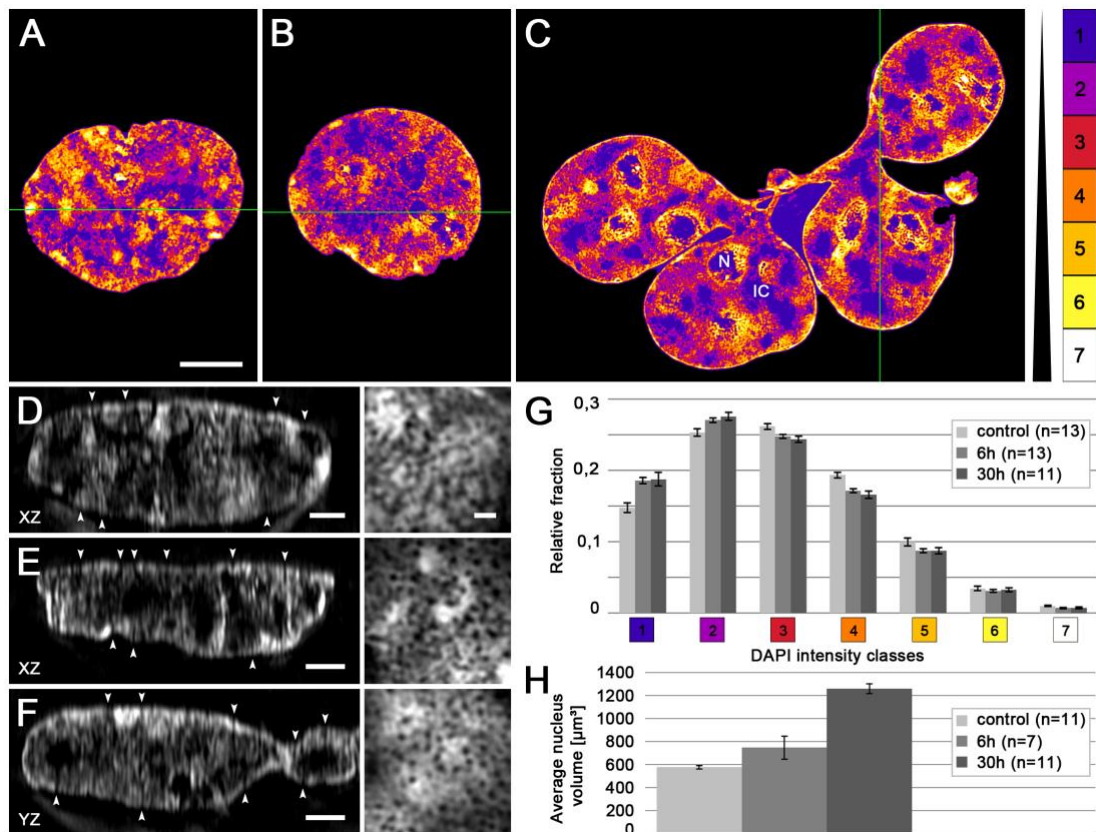
Fig. 3: Topological chromatin compaction mapping

(A-C) DAPI stained mid-sections of representative nuclei acquired by 3D-SIM from **(A)** control nucleus; **(B)** Cohesin depleted nucleus (6h auxin); **(C)** Cohesin depleted multilobulated nucleus (MLN) (30h auxin). Chromatin compaction of nuclei based on seven DAPI intensity classes is displayed in false colors. Class 1 (*blue*) represents pixels close to background intensity, largely reflecting the interchromatin compartment (IC), class 7 (*white*) pixels with highest intensities. All nuclei in A-C reveal a network of chromatin domain clusters (CDCs) comprising a compacted core and a surrounding low-density layer co-aligned with class 1 regions that meander between CDCs as part of the IC. Likewise, all nuclei display a rim of compacted (hetero)chromatin at the nuclear periphery and around nucleoli. N = nucleolus; IC = interchromatin channels/lacunae. The green lines indicate the section plane for xz/yz cross sections of the respective nuclei shown in (D-F). Scale bar: 5 µm. **(D-F)***(left column):* cross sections from nuclei shown in (A-C) demonstrate connections from the IC with nuclear pores (arrowheads); *(right column):* nuclear pores from respective nuclei shown in apical z–sections. Scale bars: 2 µm in cross sections; 0.5 µm in apical z-sections; **(G)** Relative 3D signal distributions of DAPI intensity classes in control nuclei, in 6h auxin treated nuclei and 30h auxin treated MLN reveal an overall similar profile for each series, yet with a relative increase of classes 1 and 2 (p<0.05 for control vs 6h and 30h auxin) and a relative decrease of classes 3 and 4 (p<0.05 for control vs 6h and 30h auxin) in cohesin depleted nuclei. *Error bars*= standard error of the mean (SEM) **(H)** Average nuclear volumes from the same series of nuclei show an increase of nuclear volumes after cohesin depletion. Note that MLN after 30h auxin are assumed to contain the double DNA amount compared to controls (for statistical tests and significance see Suppl_Table 1).

12

270   For a quantitative mapping of functionally relevant markers on DAPI intensity classes,

271   we performed immunostaining of SC35, an integral protein of splicing speckles, involved in co-

272   transcriptional splicing and transcriptional elongation [35, 36], of RNA Pol II, phosphorylated

273   at Ser5, representing the transcription initiating form of RNA Pol II [37], and of histone

274   H3K27me3 conveying a repressed chromatin state [38] (Fig. 4). SC35 was greatly enriched in

275   the IC (intensity class1), while H3K27me3 chromatin was preferentially located in higher

276   compacted CDs of both controls and cohesin depleted nuclei (Fig. 4A-C). RNA Pol II was

277   enriched in the PR, i.e. decondensed chromatin lining the IC (Fig. 4D-F). Notwithstanding the

278   significantly different distributions of SC35, RNA Pol II and H3K27me3 with regard to the seven

279   DAPI intensity classes, a highly similar distribution was found for each marker both in controls

280   and pre- and postmitotic cohesin depleted cells (Fig. 4G,H).

13
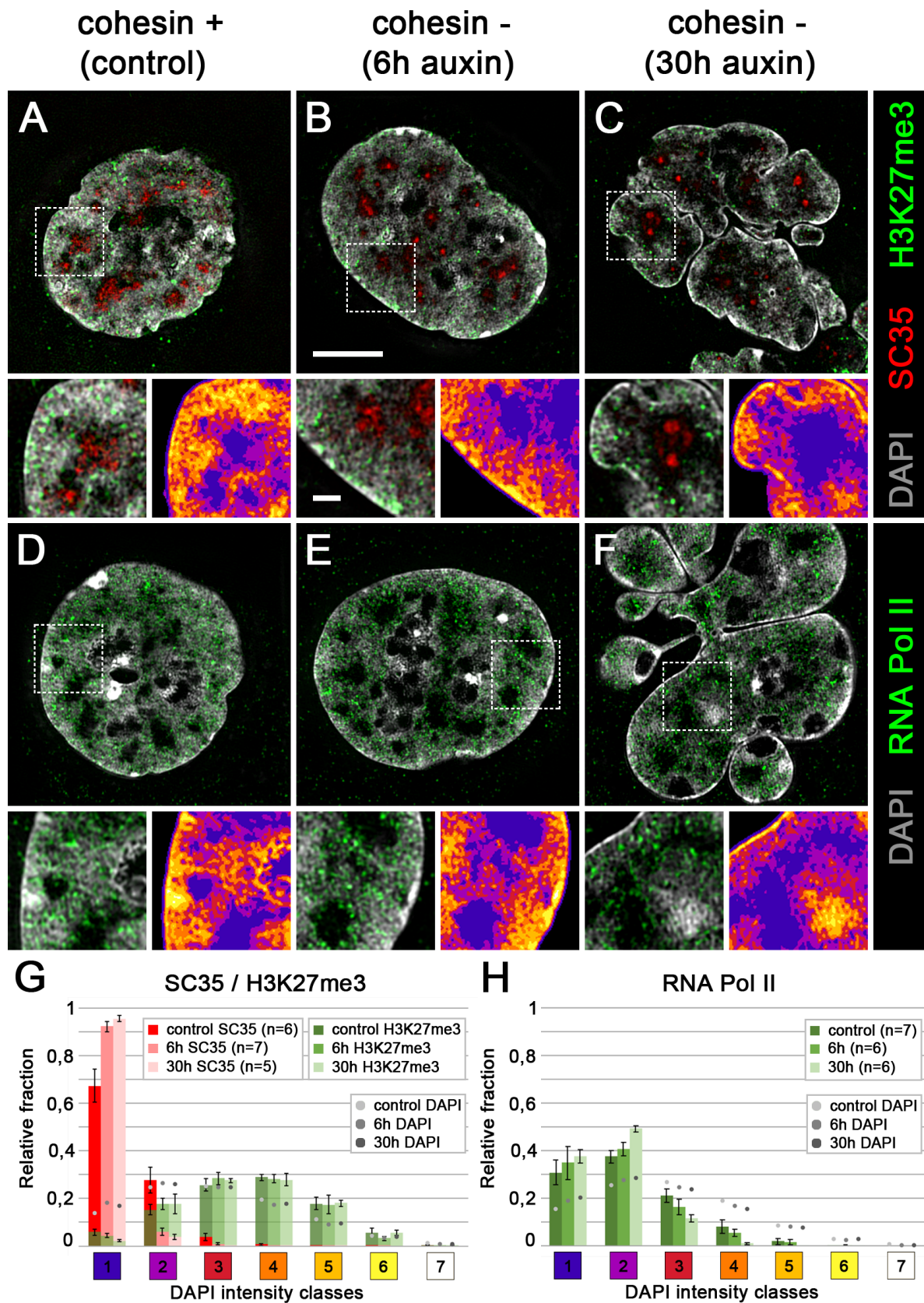
Fig. 4: Maintenance of the 3D topography in cohesin depleted nuclei for nuclear markers SC35, H3K27me3 and active RNA Pol II on chromatin compaction maps

**(A-F)** SIM optical mid-sections from whole 3D acquisitions of DAPI stained nuclei (gray) with representative zoomed magnifications also displayed as classified DAPI intensity heat maps. **(A-**

14

286 **C)** Immunostaining of SC35 (red) and H3K27me3 (green), **(D-F)** of active RNA Pol II with

287 (A,D)=controls, (B,E) = 6h auxin treatment, (C,F) = postmitotic MLN after 30h auxin treatment.

288 SC35 is mostly seen in class 1 reflecting the interchromatin compartment (IC), H3K27me3 is

289 enriched in more compacted chromatin regions (classes 3-5). RNA Pol II shows a preferential

290 localization at decondensed chromatin sites lining the IC in D-F. Scale bar: 5 μm in mid-sections;

291 1 μm in insets. **(G)** Relative signal distribution of SC35 (red) and H3K27me3 (green), **(H)** of active

292 RNA Pol II (green) on DAPI intensity classes 1-7 (DAPI distribution is marked as gray dots). The

293 different color shades denote controls, 6h auxin and 30h auxin treated cells. With exception for

294 SC35 in controls and cohesin depleted nuclei marker distributions between controls and cohesin

295 depleted nuclei do not show significant differences (for statistical tests and significance see

296 Suppl_Table 1).

297

298 *In situ Hi-C data indicate a consistent disappearance of chromatin loops in cohesin depleted*

299 *pre- and postmitotic nuclei but maintenance of A and B compartments*

300 *In situ* Hi-C confirmed the disappearance of loop domains previously described in cohesin

301 depleted premitotic cells [18, 20] also in postmitotic cell cultures, which were treated with auxin

302 for 28h before fixation (Fig. 5A). In these cultures, most cells carried MLN (compare

303 suppl_Fig.3). A and B compartments are reconstituted in these postmitotic MLN (Fig. 5B). A

304 heightened compartmentalization was noted in particular in B-type chromatin of MLN, as

305 previously described for premitotic cohesin depleted cells [18]. Even in our low depth data from

306 28h auxin treated postmitotic MLN cells, the strengthened interactions between this B-type

307 subcompartment could be readily observed (Fig. 5C,lower right panel). While the functional

308 identity or significance of this particular B-type subcompartment remains unknown, by k-means

309 clustering of histone modification data for HCT116-RAD21-mAC cells [18], we were able to

310 identify a histone modification cluster (consisting of depletion of both activating marks like

311 H3K36me3 and H3K27Ac and repressive marks such as H3K27me3 and H3K9me3, but a mild

312 enrichment of H3K79me2) that corresponded to the positions of this particular B-type

313 subcompartment (Fig 5D).
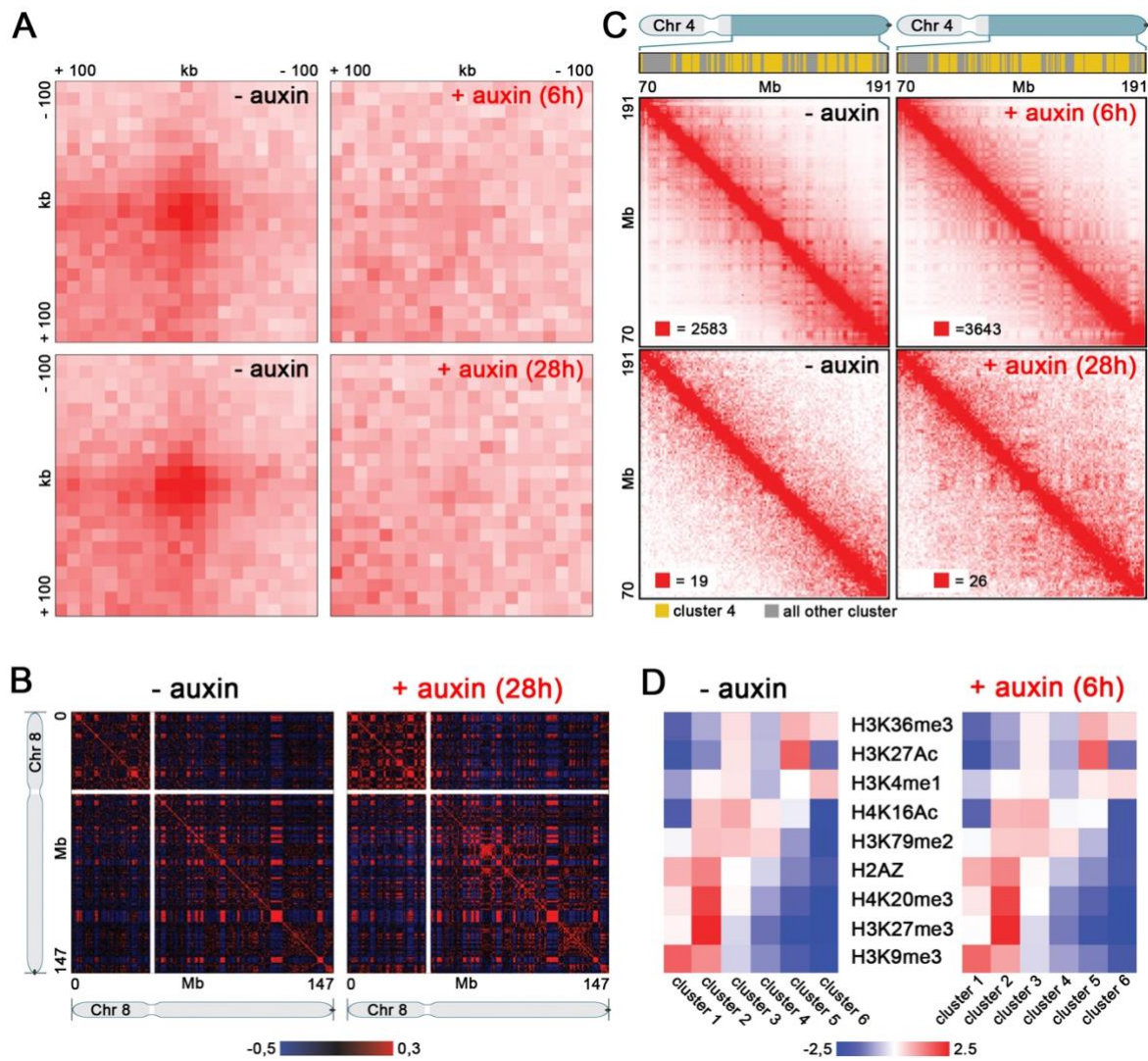
15

Fig. 5: Hi-C data indicate elimination of chromatin loops, but maintenance of A and B compartments in cohesin depleted pre- and postmitotic cells

(A) Aggregate peak analysis **(**APA) plots using loops identified in HCT116-RAD21-mAC cells [18] before and after 6h of auxin treatment (top) or before and after 28h of auxin treatment (bottom). The plot displays the total number of contacts that lie within the entire putative peak set at the center of the matrix. Loop strength is indicated by the extent of focal enrichment at the center of the plot. **(B)** Pearson's correlation maps at 500 kb resolution for chromosome 8 before (left) and after (right) 28h of auxin treatment. The plaid pattern in the Pearson's map, indicating compartmentalization, is preserved in cohesin depleted nuclei even after 28h of auxin treatment. **(C)** Contact matrices for chromosome 4 between 70 Mb and 191 Mb at 500 kb resolution before (left) and after (right) cohesin depletion. The 6h cohesin depletion time is shown on top, and 28h depletion time on the bottom. Interactions for loci in cluster 4 (annotated in yellow on top tracks) are strengthened after both 6h or 28h of cohesin depletion. All loci belonging to clusters other than cluster 4 are annotated in gray in the top track. **(D)** Clustering of histone modifications at 25 kb resolution into six clusters reveals consistent clusters of histone modification before and after cohesin depletion. For each cluster, the average log2-fold enrichment for each histone modification over all loci in that cluster is shown.

16

332

Same replication timing for cohesin depleted and non-depleted control cells seen by Hi-C and

Repli-Seq data

Using Repli-Seq and Hi-C analysis replication timing was measured by the ratio of early to late

replicating DNA and was found preserved upon cohesin depletion (Suppl_Fig. 5A,B).

Additionally, the tight relationship between genome A/B compartmentalization and replication

timing was similarly maintained in the absence of cohesin (Suppl_Fig. 5C).

Persistence of typical S-phase stage replication patterns after cohesin depletion and their

restoration in postmitotic MLN

The temporal order of DNA replication occurring at distinct replication sites as replication foci

is highly coupled with genome architecture, resulting in typical patterns for early, mid and late

replication timing [39]. These replication sites persist as stable chromatin units (replication

domains, RDs) throughout interphase and during subsequent cell cycles [40-43] and were

chosen in our study as reference structures for CDs (see Discussion). Replicating DNA was

visualized by pulse replication labeling (RL), using an approach where fluorophore-conjugated

dUTPs are incorporated by a short scratch of S-phase cells [42, 44]. RDs could then be

visualized through the remaining and the next cell cycle without further detection steps. Images

were acquired by 3D-SIM.

RD patterns were recorded in cells with the following culture conditions: Control

cultures were fixed 6h after RL (Fig. 6A). Cultures prepared for cohesin depletion were further

grown after RL for 1h under normal medium conditions and then exposed to auxin for 6h (Fig.

6B,C) or 30h respectively (Fig. 6D), before fixation. Both, controls and auxin-treated cells

revealed typical RD patterns for all S-phase stages. Fig. 6C shows a labeled nucleus that has

entered mitosis. Our observations demonstrate that a given RD pattern not only persists during

the subsequent interphase and along mitotic chromosomes (Fig. 6B,C) but can also be fully

reconstituted after mitosis in MLN (Fig. 6D).

Moreover we showed that *de novo* DNA synthesis with the formation of typical

replication patterns still occurs in cohesin depleted postmitotic MLN. Fig. 6E shows examples

361   where RL was performed under continuous auxin treatment in cells that were kept in auxin for

362   30h prior to RL.

363
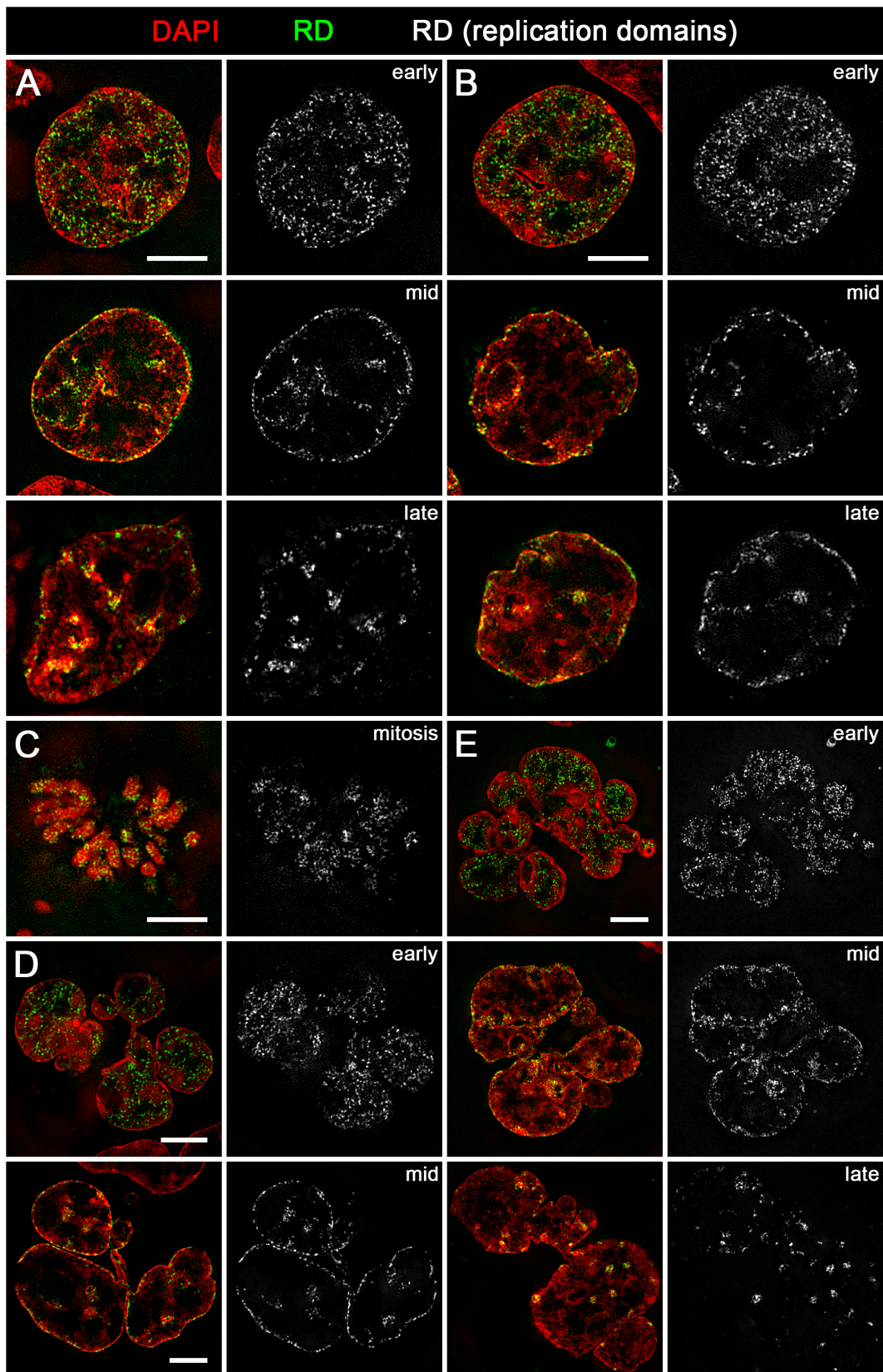
Fig. 6: Maintenance, postmitotic re-establishment and de novo formation of typical replication patterns after cohesin depletion

366 **(A-E)** Representative SIM sections of DAPI stained nuclei (red) with replication domains (RDs,

367 green in overlay images) in different cell cycle stages. Respective RDs are in addition separately

368 shown in gray. **(A)** Control nuclei fixed 6h after replication labeling (RL) delineating the typical

369 patterns for early, mid and late replication. **(B)** Maintenance of typical replication patterns in cohesin

370 depleted nuclei. For complete cohesin depletion nuclei were incubated for 6h in auxin after

371 replication labeling performed in normal medium conditions. **(C)** Mitosis with RDs emerging from a

372 replication labeled nucleus under conditions as described in (B). **(D)** Replication patterns in a

373 postmitotic multilobulated nucleus (MLN). RL was performed in normal medium conditions and cells

374 subsequently treated with auxin for 30h. Re-established RDs form typical early and mid-to-late

375 replication patterns in individual lobuli. **(E)** *De novo* DNA synthesis with formation of typical

376 replication patterns in MLN. Cells were treated with auxin for 30h prior to replication labeling under

377 continuous auxin conditions. Scale bar: 5 µm.

378

Individual replication domains (RDs) and DNA halo induced chromatin loops are enlarged in cohesin depleted cells

381 Finally, we tested whether cohesin depletion following RL during early S-phase results in

382 numerical and/or structural changes of individual RDs (Fig. 7). We compared numbers of

383 segmented RDs plotted as the mean value of counts / nucleus (Fig. 7B) and the total volumes

384 of all segmented RDs, plotted as the mean total RD volume / nucleus (Fig. 7C) between control

385 nuclei grown for 6h after RL in normal medium conditions, premitotic nuclei grown for 6h in

386 auxin after RL, and postmitotic MLN grown for 30h in auxin after RL. Both, total volumes and

387 counts of segmented RDs were higher in cohesin depleted nuclei and slightly increased with

388 the duration of auxin induced degradation of cohesin, hinting to chromatin relaxation at the

389 level of individual RDs.

19
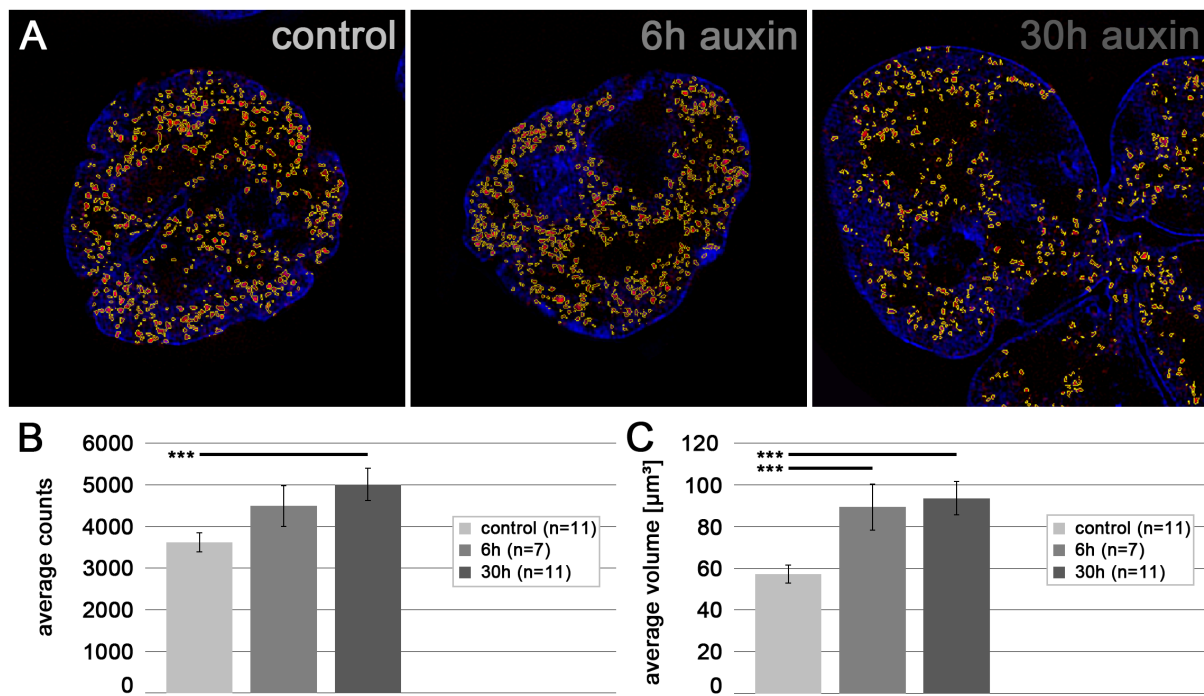
Fig. 7: Segmentation of individual replication domains established in early S-phase

(A) SIM optical mid-sections of DAPI stained nuclei (blue) from a control *(left)*, a 6h auxin treated nucleus *(mid)* and a 30h auxin treated MLN *(right)*. Replication labeling was performed prior to cohesin depletion. RDs are displayed in red with segmented borders lined in yellow. The lower density of RDs in the postmitotic MLN is clearly evident. **(B)** Average counts of segmented RDs plotted as the mean value of object counts / nucleus in each series. **(C)** Volumes of segmented RDs plotted as the mean total volume of RDs/nucleus in each series. Significance (p<0.05) between series indicated by asterisks. Scale bar: 4 µm

An effect of cohesin depletion on RD structure was supported by a DNA halo approach, a technique to investigate changes in chromatin organization at the level of DNA loops [45]. Histone extraction in interphase nuclei by high-salt incubation triggers the extrusion of chromatin loops from a densely stained central chromatin core thus providing a measure of their size. DAPI stained nuclei of cohesin depleted cells (6h auxin treatment) exhibited halos that were significantly larger and more variable in shape in comparison to the defined and compacted halos of control cells (Suppl_Fig. 6).

20

Discussion

Perturbed mitoses with formation of a single postmitotic multilobulated nucleus (MLN) in cohesin depleted cells

Our Repli-Seq data and live cell observations confirm an undisturbed cell cycle progress of cohesin depleted cells towards mitosis [28] and a disturbed course of mitotic progress [46]. In addition our time lapse observations reveal a so far unreported arrest of telophase in conjunction with a lack of cytokinesis, resulting in a single postmitotic cell harboring one MLN. Several factors may contribute to this outcome: cohesin loss was previously shown to prompt a defect of centrosome duplication and spindle pole integrity, as well as a compromised cohesin-mediated kinetochore-microtubule attachment [46] (reviewed in [1, 2]). Notably, in vertebrates cohesin is loaded onto DNA already in telophase [1, 5], which may be relevant for correct cytokinesis and daughter cell formation. Loss of cohesin is, however, not mandatory for the formation of MLN. MLN are found in cells with a mutant CTD Thr4-phosphorylation in a mitosis-specific form of RNA Pol II [47]. Multilobulation also arises in terminally differentiated granulocytes [48] and in tumor cells with extensive chromosomal rearrangements, such as Hodgkin lymphoma associated Reed-Sternberg cells [49]. Our observation of MLN as the mitotic outcome in ~2% of HCT116-RAD21-mAC control cells exemplifies the spontaneous occurrence of MLN in a near-diploid tumor cell line. Overall, the complex interactions of factors promoting MLN are still poorly understood [50, 51].

Maintenance of principle features of higher order chromatin architecture in cohesin depleted nuclei in line with the ANC-INC model

Hallmarks of the ANC-INC model (reviewed in [23-25], see Introduction) were retained in cohesin depleted pre- and postmitotic cell nuclei. These hallmarks include the preservation of chromosome territories (CTs), chromatin domain clusters (CDCs) structurally organized by different compaction levels, an interchromatin (IC) channel system and the maintenance of an active compartment (ANC), represented by markers for transcriptional competence (here active RNA Pol II and splicing speckles) and a co-aligned inactive compartment (INC) with

439   repressed chromatin (H3K27me3).

440   We also examine replication domains (RDs). RDs defined by genome-wide Repli-Seq

441   analyses are often considered to correspond to TADs mapped by Hi-C methods [27, 52] and

442   as molecular equivalents of replication foci / domains observed by microscopic methods [53].

443   Yet, a direct comparison of these structures is a delicate issue since neither RDs nor TADs

444   are strictly defined: microscopically observable replication sites were initially reported in rat

445   fibroblast nuclei with an average DNA content of ~1 Mb [54]. Later studies with conventional

446   and super-resolution microscopy [40, 44, 55] showed that RDs with an average DNA content

447   of 400–800 kb [56] can be optically resolved down to a few single replicons (150–200 kb)

448   clustered per replication site. Similarly, the definition of TADs with a size range of ~0.1-1Mb

449   (and further grouping into subTADs and metaTADs) has remained somewhat fuzzy, likely due

450   to their dynamic behavior [57], differences of evaluation mode and interpretation [58, 59].

451   A recent review rejected the above hierarchy of metaTADs, TADs, and subTADs, and

452   instead argued for a very different classification of contact domains into two types [60]:

453   compartmental domains which originate due to the co-segregation of chromatin intervals with

454   similar marks, and loop domains, which emerge from cohesin extrusion.

455   Critically, in our study, we report the maintenance of replication domains (RDs) in

456   cohesin depleted nuclei over mitosis with re-formation of typical patterns for all S-phase stages

457   in postmitotic MLN. Thus, replication domains remain despite the loss of all loop domains

458   (whether classified as TADs, subTADs, metaTADs, etc). Instead, we find that the boundaries

459   of replication domains align with the boundaries of compartmental domains. Thus, our work is

460   consistent with the view that there are two types of domains. Compartmental domains, which

461   do not depend on cohesin extrusion, correspond closely to replication domains. By contrast,

462   loop domains, which result from cohesin extrusion, do not correspond to the boundaries of

463   replication domains.

464

465   *Disappearance of loop domains and concomitant persistence of functional higher order*

466   *chromatin arrangements underpins different mechanisms for their structural organization*

467   The disappearance of chromatin loops as basic chromatin folding structures demonstrated by

468   Hi-C experiments may lead to the expectation of a profound effect on the global higher order

469   chromatin organization, like a house of cards falling together when a basal card is removed.

470   Apparently, this is not the case as has been previously shown by the maintenance and even

471   strengthening of compartmentalization into A and B domains after cohesin depletion [18, 20].

472   In the present study the persistence of compartment domains was also demonstrated for

473   cultures highly enriched with postmitotic MLN.

474   Chromatin loop domains are formed by means of an extrusion mechanism where by

475   the gradual expansion of a loop through a cohesin ring two opposite CTCF sites are tethered

476   together and anchored at CTCF/cohesin binding sites (reviewed in [6, 61-64]). These anchor

477   sites manifest as bright peaks in Hi-C maps. Based on cohesin depletion experiments this loop

478   extrusion mechanism was shown to be cohesin dependent ([18, 20, 21] and this study).

479   Elimination of cohesin dependent chromatin loop domains visualized in Hi-C maps by the

480   respective disappearance of squares of enhanced contact frequencies does, however, not

481   necessarily reflect a complete loss of chromatin loops. An effect of cohesin depletion on

482   chromatin decompaction / relaxation with a modest increase of RD diameters as found in our

483   present study may already result in a major decrease of 3D contact frequencies and contribute

484   to the failure to detect loop domains. Our observation that replication foci become physically

485   larger after cohesin depletion also suggests cohesin dependent extrusion may play a role in

486   the physical compaction of replicating chromatin. This is consistent with a model where

487   cohesin extrusion tends to compact intervals of replicating chromatin, but where their genomic

488   boundaries are associated with compartmentalization [29].

489   Moreover, cohesin rings as chromatin loop anchors may in part be replaced after

490   cohesin depletion by other factors with less defined anchor points (reviewed in [6, 7, 63]). The

491   entrance of cells into mitosis provides a case in point for a structural change of chromatin loop

492   organization which prompts a loss of the Hi-C plaid or check-board pattern in mitotic

493   chromosomes [65]: upon entering mitosis, cohesin is lost from chromosome arms (reviewed

494   in [1]) and helically arranged nested loop arrays are formed by condensins I and II. The

495   organization of chromatids in mitosis can be described as a linearly organized, longitudinally

496 compressed array of consecutive chromatin loops [66]. Notwithstanding this major change of

497 chromatin loop organization between interphase and mitosis, major features of higher order

498 chromatin organization persist and are transmitted from one cell cycle to the next [67, 68].

499 Chromatin loop clusters attributed to distinct CDs during interphase continue to be present in

500 close spatial arrangements along mitotic chromosomes which allows the rapid re-

501 establishment of loops, domains and compartments early in G1.

502 Cohesin-independent maintenance of Hi-C detectable A and B compartments was

503 reported in several studies (reviewed in [22]). In line with only minor effects of cohesin depletion

504 on gene expression [18], the present study underpins that mechanisms that direct the

505 maintenance of individual RDs and their spatio-temporal order, as well as the spatial

506 arrangement of higher order chromatin organization in the context of the ANC-INC model are

507 also independent of cohesin and sufficient to instruct accurate reformation of these structures

508 upon exit from mitosis into a subsequent cell cycle in the absence of cohesin. We argue that

509 RDs correspond with compartment domains in line with [29] where discrete cis-regulatory

510 elements which orchestrate domain-wide replication timing, A/B compartmentalization and

511 loop architecture, were identified.

512

513 **An integrated view of the functional nuclear landscape based on Hi-C and microscopic**

514 **data**

515 Although microscopically derived distance maps were reported in excellent agreement with Hi-

516 C maps [69], Hi-C and microscopy yield different views on the nuclear landscape and

517 unexplored gaps between findings obtained with these approaches have to be closed. Hi-C

518 has made possible the genome wide identification of the spatial proximity of DNA segments in

519 cis and trans [12-14, 70] and genome wide data on chromatin modifications and architectural

520 proteins mapped along the DNA can be easily integrated into the resulting architectural

521 landscape. However, as a method based on 3D DNA-DNA contact frequencies Hi-C lacks the

522 power to identify the system of IC-channels and the lining PR. These features have been

523 demonstrated consistently in many cell types and species with super-resolved microscopy [24,

524 25]. The relationship of compartments A and B identified by Hi-C with the co-aligned

24

525   compartments described by the ANC-INC model has not yet been clarified. Some studies

526   traced genomic features within a range of few Mb with a combination of super-resolved

527   microscopy and Hi-C [71, 72]. Using stochastic optical reconstruction microscopy, Bintu et al.

528   [71] demonstrated domain-boundary-like structures in single cohesin depleted nuclei. Loss of

529   cohesin, however, abolished preferential boundary sites with a corresponding loss of loop

530   domains detectable by Hi-C at the population-average level in cohesin depleted cells.

531   Furthermore, Hi-C is not an appropriate method to measure absolute chromatin

532   compaction. Simply put, Hi-C does not measure absolute contact frequency, and 3D

533   reconstructions of higher order chromatin organization from Hi-C data have sometimes been

534   used to argue for relatively open and accessible lariat-like chromatin loop structures [69, 73-

535   76]. In contrast, recent studies using advanced microscopic strategies have suggested

536   nucleosome clusters (NCs) as basic entities of chromatin organization beyond the nucleosome

537   level [77-79]. Chromatin loops built from NCs imply more compacted and less accessible CDs

538   with profound consequences for their accessibility for macromolecules (see below). Cartoons

539   of 3D TAD structures [69, 73-76] suggest an unconstrained access of individual

540   macromolecules, such as transcription factors, into the interior and also a constrained

541   accessibility of macromolecular complexes. In contrast, we and others [80] consider the

542   possibility that the accessibility of CDs may be impeded to an extent that the diffusion of

543   individual macromolecules is constrained, and macromolecular complexes are fully excluded.

544   We postulate that this basic organization is maintained in cohesin depleted nuclei.

545

546   **Outlook**

547   The polymer melt model of the CD structure proposed by Maeshima and colleagues [81]

548   argues for dense packaging of ~10 nm thick chromatin fibers in the interior of CDs. Based on

549   Monte Carlo simulations Maeshima et al. [80] proposed that nucleosome densities >0.3 to 0.5

550   mM, corresponding to DNA densities of ~40 – 60 Mb/μm$_3$, result in an accessibility barrier for

551   molecule complexes with diameters >20 – 25 nm. Estimates of DNA densities based on super-

552   resolved microscopy of CDs in various human and mouse cell nuclei indicate a range in the

553   order of 5 - 200 Mb/μm$_3$ (C. Cremer, unpublished data). These estimates argue for an

554　exclusion of macromolecular complexes from the interior of CDs with higher compaction levels

555　and thus favor models proposing that macromolecular complexes involved in transcription and

556　other important nuclear functions act at the periphery of CDs [24, 25, 80, 82]. The implications

557　of this model for the mobility of CDs and functional DNA targets have remained elusive. In line

558　with current views of chromatin organization based on the formation of chromatin droplets with

559　distinct chromatin states [60], a recent Hi-C based genome-wide model depicts contact

560　domains and TADs as separated chromatin balls [83]. We have postulated that the IC may

561　provide preferred routes for imported transcription factors to their target sites, for the

562　intranuclear passage of regulatory RNAs to remote functional sites, and for export routes of

563　mRNPs towards nuclear pores [25]. In order to test this hypothesis, it is necessary to explore

564　the space-time compaction and accessibility of CDs. Super-resolved fluorescence microscopy,

565　including single molecule localization microscopy (SMLM) and stochastic optical

566　reconstruction microscopy (STORM), may become the methods of choice to measure absolute

567　differences of DNA/chromatin compaction with spatial resolution at the nanometer scale [79,

568　84, 85], whereas chromatin accessibility can be probed indirectly with methods that allow to

569　measure molecular diffusion rates [86-89].

570

571　**Materials & Methods**

572　*Cells and culture conditions*

573　HCT116-RAD21-mAID-mClover cells (referred to as HCT116-RAD21-mAC cells in the

574　manuscript) were generated and kindly provided by the Kanemaki lab (Mishima Shizuoka,

575　Japan; [16]). For a detailed description see Suppl_Fig. 1. Cells were cultured in McCoy's 5A

576　medium supplemented with 10% FBS, 2 mM L-glutamine, 100 U/ml penicillin, and 100 µg/ml

577　streptomycin at 37°C in 5% CO_2.

578

579　*Auxin induced RAD21 proteolysis*

580　Degradation of the AID-tagged RAD21 was induced by addition of auxin (indole-3-acetic acid;

581　IAA, Sigma Aldrich) to the medium at a final concentration of 500 µM (auxin stock solution 2

582　M in DMSO). In long term cultures fresh auxin-medium was added after 20-24h.

583

584　*Immunodetection*

585 Cells were grown on high precision coverslips (Roth, LH22.1, #1.5) to 80% confluency and

586 washed two times in PBS before fixing them in 2% formalin/PBS for 10 min. After a stepwise

587 formalin exchange with PBS/Tween 0.02%, cells were permeabilized with 0.5% Triton X-

588 100/PBST for 10 min and then incubated in 2% BSA/PBST as blocking solution for 1h to

589 minimize non-specific antibody binding. For immunodetection, primary and secondary

590 antibodies were diluted in blocking solution and incubated each for 1h in a dark humified

591 chamber to prevent drying and fluorescence fading. Primary antibodies against cohesin

592 subunits RAD21, SMC1, SMC3 (Abcam), all raised in rabbit, were detected with Cy3-

593 conjugated goat anti rabbit antibodies (Abcam). Primary antibodies against SC35 (Sigma),

594 RNA Pol II (Abcam) and H3K27me3 (Active Motif) were detected with either donkey anti mouse

595 Alexa 488 (Life technologies) or donkey anti rabbit Alexa 594 (Life technologies). A postfixation

596 step in 4% formalin/PBS helped to stabilize bound antibodies. Cells were counterstained in 1

597 µg/ml DAPI, mounted in antifade mounting medium Vectashield (Vector Laboratories) and

598 sealed with nail varnish (for details see [90]).

599

600 *Replication pulse labeling*

601 *1. replication scratch labeling:* Cells cultivated on high precision coverslips (thickness 0.170

602 mm) grown to 50-80% confluency were transferred into a dry empty tissue dish after draining

603 off excess medium. 30 µl of the prewarmed labeling solution (20 µM Cy3-dUTP (homemade)

604 or Alexa 594-5-dUTP (Life technologies)) was evenly distributed over the coverslip. With the

605 tip of a hypodermic needle parallel scratches at distances of ~100 µm were quickly applied to

606 the cell layer. Cells were incubated for 1 min in the incubator, then a few ml of pre-warmed

607 medium was added to the dish. After 30 min medium was exchanged to remove non-

608 incorporated nucleotides (for details see [42, 91]). Avoidance of any chemical treatments

609 preserves the RAD21-mClover fluorescence after labeling and was therefore used for all RL

610 experiments with exception for the labeling experiment shown in Fig. 6E.

611

612 *2. Incorporation of 5-Ethynyl-dU (EdU) and detection by „click chemistry"*

613 This approach was used for RL in MLN since these cells are prone to detachment upon

614 scratching (compare Fig. 6E) taking the degradation of the protein-tagged RAD21-mClover

615 fluorescence caused by the acidic reaction [92]. EdU was added at a final concentration of 10

616 µM to the medium for 15min. Incorporated EdU was detected according to manufactures

617 instructions (baseclick) by a Cu(I) catalyzed cycloaddition reaction that covalently attaches a

618 fluorescent dye containing a reactive azide group to the ethynyl-group of the nucleotide [93].

619 For visualization of RDs, the dye 6-FAM-Azide (baseclick) at a final concentration of 20 µM

620 was used.

621 After either labeling approach cells were washed in 1xPBS and fixed with 4% formaldehyde /

622 PBS for 10 min. After a stepwise exchange with PBST, cells were permeabilized with 0.5%

623   Triton X-100/PBS/Tween 0.02% for 10 min and washed again in 1xPBS. Cells were

624   counterstained in 1 µg/ml DAPI and mounted in antifade mounting medium Vectashield (Vector

625   Laboratories); for details see [90]).

626

627   *HI-C in situ analysis of untreated and auxin treated cells*

628   HCT-116-RAD21-mAC cells were plated in 6 well plates with either complete media, or

629   complete media with 500uM auxin (IAA) for 6 hours (as in [22]) or 28 hours (to enrich for post-

630   mitotic cells with multilobulated nuclei). Cells were crosslinked with 1% formaldehyde directly

631   on the plate for 10 minutes and then quenched with glycine. The crosslinked cells were then

632   scraped off and *in situ* Hi-C was performed as in [14]. In brief, cells were permeabilized with

633   nuclei intact, the DNA was digested overnight with MboI, the 5'-overhangs were filled in while

634   incorporating bio-dUTP, and the resulting blunt end fragments were ligated together.

635   Crosslinks were then reversed overnight, the DNA was sheared to 300-500bp for Illumina

636   sequencing, biotinylated ligation junctions were captured using streptavidin beads and then

637   prepped for Illumina sequencing. We prepared 3 libraries (two biological replicates) each for

638   each time point (untreated 6 hours, treated 6 hours, untreated 28 hours, treated 28 hours). All

639   Hi-C data was processed using Juicer [94, 95]. The data was aligned against the hg19

640   reference genome. All contact matrices used for further analysis were KR-normalized with

641   Juicer. Comparison of compartment strengthening to histone modification clusters was done

642   as in [22]. Histone modification data for 9 marks (H3K36me3, H3K27Ac, H3K4me1, H4K16Ac,

643   H3K79me2, H2AZ, H4K20me3, H3K27me3, H3K9me3) generated from untreated and 6-hour

644   treated cells in [22] was grouped into 6 clusters using k-means clustering. For the k-means

645   clustering, the histone modification data was first converted into a z-score value for each mark

646   in order to account for differences in the dynamic range between marks.

647

648

649   *Repli-Seq of untreated or auxin-treated cells*

650   HCT116-RAD21-mAC cells were synchronized in G1 with lovastatin as previously described

651   [96]. Briefly, cells were incubated with 20 µM Lovastatin (Mevinolin) (LKT Laboratories M1687)

652   for 24 hours to synchronize in G1. 500 µM auxin or DMSO was added 6 hours before release

653   from lovastatin block. To release from G1 block, lovastatin was washed away with 3 washes

654   of PBS and warm media plus 2 mM Mevalonic acid (Sigma-Aldrich M4667) and 500 µM Auxin

655   or DMSO. Cells were released for 10, 14, 18, and 22 hours. 2 hours before the time point 100

656   µM BrdU was added to label nascent replication. After fixation, equal numbers of cells from

657   each release time point were pooled together for early/late repli-seq processing [97]. Repli-

658   Seq data was processed as described in [97]. In brief, data was aligned to the hg19 reference

659   genome using bowtie2, deduplicated with samtools, and the log-2 ratio between early and late

660   timepoints was calculated.

661

662

663 *3D DNA-FISH*

664 Hapten - or directly labeled chromosome painting probes delineating human chromosomes 4-

665 (BIO), 12-(DIG) and 19-Cy3, generated from flow sorted chromosomes as previously

666 described in detail [30] were kindly provided by Stefan Müller (LMU). 30 ng of each labeled

667 probe and a 20-fold excess of COT-1 DNA was used per 1 µl hybridization mix (50%

668 formamide/ 2xSSC/ 10% dextran sulfate).

669 Cells were washed in 1xPBS and fixed with 4% formaldehyde/PBS for 10 min. After a stepwise

670 exchange with 0.5% Triton X-100/PBS, cells were permeabilized with 0.5% Triton X-100/PBS

671 for 10 min, washed in 1xPBS. Further pretreatment steps included incubation in 20% glycerol

672 (1h), several freezing/thawing steps in liquid N_2, and incubation in 0.1 N HCl (5 min). Cells

673 were stored in 50% formamide/2xSSC overnight. After simultaneous denaturation of probe and

674 cells (2 min at 76°C), hybridization was performed at 37°C for 48h. After stringent washing in

675 0.1xSSC at 60°C, biotin was detected by streptavidin-Alexa 488 and DIG by a mouse-anti-DIG

676 antibody conjugated to Cy5. Cells were counterstained in 1 µg/ml DAPI, mounted in antifade

677 mounting medium Vectashield (Vector Laboratories) and sealed with nail varnish (for details

678 see [30]).

679

680 *DNA halo preparation*

681 HCT116-RAD21-mAC cells were incubated for 6h in 500 µM auxin for cohesin depletion. DNA

682 halo preparation was largely performed according to [98]. After washing the cells in 1xPBS

683 they were incubated for 10 min in a buffer at 4°C containing 10 mM Tris pH 8, 3 mM $MgCl_2$,

684 0.1 M NaCl, 0.3 M sucrose, protease inhibitors (freshly added to the buffer prior to use) 1 µM

685 pepstatin A, 10 µM E64, 1 mM AEBSF and 0.5% Nonidet P40. All the following procedures

686 were performed at room temperature. Subsequently DNA was stained for 4 min with 2 µg/ml

687 DAPI. After 1 min in a second extraction buffer (25 mM Tris pH 8, 0.5 M NaCl, 0.2 mM $MgCl_2$;

688 protease inhibitors as in nuclei buffer and 1 mM PMSF were added fresh prior to use), cells

689 were incubated 4 min in halo buffer (10 mM Tris pH 8, 2 M NaCl, 10 mM EDTA; protease

690 inhibitors as in nuclei buffer and 1 mM DTT were added fresh prior to use). Eventually cells

691 were washed 1 min each in two washing buffers (25 mM Tris pH 8, 0.2 mM $MgCl_2$; the first

692 buffer with and the second without 0.2 M NaCl). After 10 min fixation in 4% formaldehyde/PBS,

693 cells were washed twice in 1xPBS, mounted on slides with Vectashield and sealed with nail

694 varnish.

695 Nuclear scaffolds and the faded DNA halos were imaged at a widefield microscope (Zeiss

696 Axioplan 2, 100x/1.30 NA Plan-Neofluar Oil Ph3 objective; Axiovision softare; AxioCam mRM

697 camera). Both the total area (At) and the scaffold area (As) of each cell were manually

698 segmented using the software Fiji and the DNA halo area (Ah) calculated as a subtraction of

699   the two (Ah = At – As). The DNA halo radius was subsequently derived with the formula R =

700    $\sqrt{(Ah/\pi)}$. Four biological replicates were prepared and measured. For generation of plots and

701   statistical analysis (Wilcoxon test) the software RStudio was used.

702

703   *Confocal fluorescence microscopy*

704   Confocal images were collected using a Leica SP8 confocal microscope equipped with a

705   405nm excitation laser and a white light laser in combination with an acousto-optical beam

706   splitter (AOBS) which allows tunable filtering of excitation from 470 to 670 nm and freely

707   programmable emission detection. The used confocal system has three different detectors,

708   one photomultiplier tube (PMT) and two hybrid photodetectors (HyD). The microscope was

709   controlled by software from Leica (Leica Application Suite X, ver. 3.5.2.18963). For excitation

710   of DAPI, the 405 nm laser was used. For excitation of Alexa488, Cy3, STAR635P and Cy5,

711   the white light laser was set to 499, 554, 633 and 649 nm, respectively. The emission signal

712   of DAPI was collected by the PMT (412-512 nm), the emission signals of Alexa488 (506-558

713   nm), Cy3 (561-661 nm), STAR635P (640-750 nm) and Cy5 (656-780 nm) were collected by

714   the two HyD detectors. Images were acquired with 42 nm pixel steps, 102 µs pixel dwell time

715   and 2-fold line accumulation using a Leica HC PL APO 63x/1.30 NA Glycerol immersion

716   objective. The frame size was 37 x 37 µm and the scan speed was 700 Hz. The size of the

717   confocal pinhole was 1 A.U. Confocal image z-stacks were acquired with a step size of 330

718   nm.

719

720   *Live cell microscopy for long term observations*

721   For live cell imaging, cells were plated on poly-L-Lysine-coated glass bottom 2-well imaging

722   slides (ibidi), allowing to image control and auxin-treated conditions in parallel. For DNA

723   staining cells were grown in media containing 500 nM SiR-DNA (Spirochrome) for 1h before

724   imaging. Timelapse acquisitions were carried out on a Nikon TiE microscope equipped with a

725   Yokogawa CSU-W1 spinning disk confocal unit (50 µm pinhole size), an Andor Borealis

726   illumination unit, Andor ALC600 laser beam combiner (405 nm / 488 nm / 561 nm / 640 nm),

727   and Andor IXON 888 Ultra EMCCD camera. The microscope was controlled by software from

728   Nikon (NIS Elements, ver. 5.02.00). Cells were imaged in an environmental chamber

729   maintained at 37°C with 5% CO_2 (Oko Labs), using a Nikon PlanApo 60x/1.49 NA oil

730   immersion objective and a Perfect Focus System (Nikon). Images were recorded every 15 min

731   for 21h as z-stacks with two planes and a step size of 6 µm, unbinned and with a pixel size of

732   217 nm. For excitation of mClover and SiR-DNA, the 488 and 640 nm laser lines were used,

733   respectively. Fiji software (ImageJ 1.51j) [99] was used to analyze images.

734

735   *Semi-automatic quantitative evaluation of multilobulated nuclei (MLN) / mitoses*

736 Image acquisitions were carried out on the Nikon spinning disk system described above. Using

737 a Nikon PlanApo 100x/1.45 NA oil immersion objective tiled images (3x3 with 5% overlap and

738 131 nm pixel size) were acquired for each condition to increase the number of cells per field

739 of view. Confocal image z-stacks were acquired in two planes with a step size of 6 µm in order

740 to encompass cells, in particular mitotic cells, in different plane levels. DAPI and mClover were

741 excited with 405 or 488 nm laser lines, respectively. All nuclei from each image (average 280

742 nuclei per image frame) were classified visually into morphologically normal nuclei, mitoses

743 and multilobulated nuclei (MLN). In auxin treated cells nuclei with persistent RAD21-mClover

744 fluorescence (~2%) were excluded.

745

746 *Structured illumination microscopy (SIM)*

747 Super-resolution structured illumination imaging was performed on a DeltaVision OMX V3

748 system (Applied Precision Imaging/GE Healthcare) equipped with a 100x/1.4 NA UPlan S Apo

749 oil immersion objective (Olympus), Cascade II:512 EMCCD cameras (Photometrics) and 405,

750 488 and 593 nm lasers (for detailed description see [100]). For sample acquisition oil with a

751 refractive index of RI=1.512 was used. 3D image stacks were acquired with 15 raw images per

752 plane (5 phases, 3 angles) and an axial distance of 125 nm and then computationally

753 reconstructed (Wiener filter setting of 0.002, channel specific optical transfer functions (OTFs))

754 and color shift corrected using the SoftWoRx software (Applied Precision Imaging/GE

755 Healthcare). After establishing 32-bit composite tiff stacks with a custom-made macro in

756 Fiji/ImageJ2 (http://rsb.info.nih.gov/ij/), the data were subsequently aligned again to get a higher

757 alignment precision. These images were then used for measurements in the Volocity software

758 (Perkin Elmer).

759

760 *Segmentation and quantification of replication domain (RD) signals*

761 Aligned 3D SIM image stacks were used as RGB for object counting and volume

762 measurements in the Volocity software. For each series between n=7 and n=11 nuclei were

763 measured. The image stacks were separated in their respective channels and then structures

764 were obtained and segmented separately. The segmentation of cohesin structures was

765 performed with the following software commands: 1. "Find Objects" (Threshold using: Intensity,

766 Lower: 32, Upper: 255), 2. "Separate Touching Objects" (Object size guide of 0,002 µm³) and

767 3. "Exclude Objects by Size", excluding structures < 0,005 µm³. Exclusion of signals outside a

768 selected nucleus was achieved by the commands "Intersect" and "Compartmentalize".

769 Segmentation of nuclei was realized by the following commands: 1. "Find Objects" (Threshold

770 using: Intensity), 2. "Dilate", 3. "Fill Holes in Objects" and 4. "Erode". Measured values for

771 volumes and object counts were plotted as histograms using bins for volume classes (0,01-0,4

772 µm³) and object counts within each bin. To compare different series, averaged values from all

773 nuclei of a given series were used. To confirm statistically significance the Mann-Whitney test

774 was applied for both object counts and volumes. For comparability of the results, the same

775 protocol was applied for all conditions

776

777 *Chromatin compaction classification by 3D assessment of DAPI intensity classes*

778 Nuclei voxels where identified automatically from the DAPI channel intensities using Gaussian

779 filtering and automatic threshold determination. For chromatin quantification a 3D mask was

780 generated in ImageJ to define the nuclear space considered for the segmentation of DAPI

781 signals into seven classes with equal intensity variance by a previously described in house

782 algorithm [34], available on request. Briefly, a hidden Markov random field model classification

783 was used, combining a finite Gaussian mixture model with a spatial model (Potts model),

784 implemented in the statistics software R [101, 102]. This approach allows threshold-

785 independent signal intensity classification at the voxel level, based on the intensity of an

786 individual voxel. Color or gray value heatmaps of the seven intensity classes in individual nuclei

787 were performed in ImageJ.

788

789 *Quantitative allocation of defined nuclear targets on 3D chromatin compaction classes*

790 Individual voxels of fluorescent signals of the respective marker channels were segmented

791 using a semi-automatic thresholding algorithm (using custom built scripts for the open-source

792 statistical software R http://www.r-project.org, available on request). XYZ-coordinates of

793 segmented voxels were mapped to the seven DNA intensity classes. The relative frequency

794 of intensity weighted signals mapped on each DAPI intensity class was used to calculate the

795 relative distribution of signals over chromatin classes. For each studied nucleus the total

796 number of voxels counted for each intensity class and the total number of voxels identified for

797 the respective fluorescent signals for SC35, RNA Pol II, H3K27me3 was set to 1. As an

798 estimate of over/under representations (relative depletion/enrichment) of marker signals in the

799 respective intensity classes, we calculated the difference between the percentage points

800 obtained for the fraction of voxels for a given DAPI intensity class and the corresponding

801 fraction of voxels calculated for the respective signals. Calculations were performed on single

802 cell level and average values over all nuclei used for evaluation and plotting. For a detailed

803 description see [34].

804

805

806 **Acknowledgments**

815

816

References

1. Jeppsson K, Kanno T, Shirahige K, Sjogren C: **The maintenance of chromosome structure: positioning and functioning of SMC complexes.** *Nat Rev Mol Cell Biol* 2014, **15:**601-614.

2. Mehta GD, Kumar R, Srivastava S, Ghosh SK: **Cohesin: functions beyond sister chromatid cohesion.** *FEBS Lett* 2013, **587:**2299-2312.

3. Nasmyth K, Haering CH: **Cohesin: its roles and mechanisms.** *Annu Rev Genet* 2009, **43:**525-558.

4. Nishiyama T: **Cohesion and cohesin-dependent chromatin organization.** *Curr Opin Cell Biol* 2019, **58:**8-14.

5. Peters JM, Tedeschi A, Schmitz J: **The cohesin complex and its roles in chromosome biology.** *Genes Dev* 2008, **22:**3089-3114.

6. van Ruiten MS, Rowland BD: **SMC Complexes: Universal DNA Looping Machines with Distinct Regulators.** *Trends Genet* 2018, **34:**477-487.

7. Yuen KC, Gerton JL: **Taking cohesin and condensin in context.** *PLoS Genet* 2018, **14:**e1007118.

8. Parelho V, Hadjur S, Spivakov M, Leleu M, Sauer S, Gregson HC, Jarmuz A, Canzonetta C, Webster Z, Nesterova T, et al: **Cohesins functionally associate with CTCF on mammalian chromosome arms.** *Cell* 2008, **132:**422-433.

9. Wendt KS, Yoshida K, Itoh T, Bando M, Koch B, Schirghuber E, Tsutsumi S, Nagae G, Ishihara K, Mishiro T, et al: **Cohesin mediates transcriptional insulation by CCCTC-binding factor.** *Nature* 2008, **451:**796-801.

10. Rao SS, Huntley MH, Durand NC, Stamenova EK, Bochkov ID, Robinson JT, Sanborn AL, Machol I, Omer AD, Lander ES, Aiden EL: **A 3D map of the human genome at kilobase resolution reveals principles of chromatin looping.** *Cell* 2014, **159:**1665-1680.

11. Sofueva S, Yaffe E, Chan WC, Georgopoulou D, Vietri Rudan M, Mira-Bontenbal H, Pollard SM, Schroth GP, Tanay A, Hadjur S: **Cohesin-mediated interactions organize chromosomal domain architecture.** *EMBO J* 2013, **32:**3119-3129.

12. Dixon JR, Selvaraj S, Yue F, Kim A, Li Y, Shen Y, Hu M, Liu JS, Ren B: **Topological domains in mammalian genomes identified by analysis of chromatin interactions.** *Nature* 2012, **485:**376-380.

13. Lieberman-Aiden E, van Berkum NL, Williams L, Imakaev M, Ragoczy T, Telling A, Amit I, Lajoie BR, Sabo PJ, Dorschner MO, et al: **Comprehensive mapping of long-range interactions reveals folding principles of the human genome.** *Science* 2009, **326:**289-293.

14. Dixon JR, Gorkin DU, Ren B: **Chromatin Domains: The Unit of Chromosome Organization.** *Mol Cell* 2016, **62:**668-680.

15. Szabo Q, Jost D, Chang JM, Cattoni DI, Papadopoulos GL, Bonev B, Sexton T, Gurgo J, Jacquier C, Nollmann M, et al: **TADs are 3D structural units of higher-order chromosome organization in Drosophila.** *Sci Adv* 2018, **4:**eaar8082.

16. Natsume T, Kiyomitsu T, Saga Y, Kanemaki MT: **Rapid Protein Depletion in Human Cells by Auxin-Inducible Degron Tagging with Short Homology Donors.** *Cell Rep* 2016, **15:**210-218.

17. Natsume T, Kanemaki MT: **Conditional Degrons for Controlling Protein Expression at the Protein Level.** *Annu Rev Genet* 2017, **51:**83-102.

18. Rao SSP, Huang SC, Glenn St Hilaire B, Engreitz JM, Perez EM, Kieffer-Kwon KR, Sanborn AL, Johnstone SE, Bascom GD, Bochkov ID, et al: **Cohesin Loss Eliminates All Loop Domains.** *Cell* 2017, **171:**305-320 e324.

19. Gassler J, Brandao HB, Imakaev M, Flyamer IM, Ladstatter S, Bickmore WA, Peters JM, Mirny LA, Tachibana K: **A mechanism of cohesin-dependent loop extrusion organizes zygotic genome architecture.** *EMBO J* 2017, **36:**3600-3618.

20. Schwarzer W, Abdennur N, Goloborodko A, Pekowska A, Fudenberg G, Loe-Mie Y, Fonseca NA, Huber W, Haering CH, Mirny L, Spitz F: **Two independent modes of chromatin organization revealed by cohesin removal.** *Nature* 2017, **551:**51-56.

21. Wutz G, Varnai C, Nagasaka K, Cisneros DA, Stocsits RR, Tang W, Schoenfelder S, Jessberger G, Muhar M, Hossain MJ, et al: **Topologically associating domains and chromatin loops depend on cohesin and are regulated by CTCF, WAPL, and PDS5 proteins.** *EMBO J* 2017, **36:**3573-3599.

22. Haarhuis JH, Rowland BD: **Cohesin: building loops, but not compartments.** *EMBO J* 2017, **36:**3549-3551.

23. Cremer M, Cremer T: **Nuclear compartmentalization, dynamics, and function of regulatory DNA sequences.** *Genes Chromosomes Cancer* 2019, **58:**427-436.

24. Cremer T, Cremer M, Hubner B, Strickfaden H, Smeets D, Popken J, Sterr M, Markaki Y, Rippe K, Cremer C: **The 4D nucleome: Evidence for a dynamic nuclear landscape based on co-aligned active and inactive nuclear compartments.** *FEBS Lett* 2015, **589:**2931-2943.

25. Cremer T, Strickfaden H, Cremer M, Hübner B, Silahtaroglu A, Hendzel M, Lanctot C, Cremer C: **Functional nuclear organization: The interchromatin compartment is shaped by dynamic chromatin arrangements.** *BioEssays, in press* 2019.

26. Rouquette J, Cremer C, Cremer T, Fakan S: **Functional nuclear architecture studied by microscopy: present and future.** *Int Rev Cell Mol Biol* 2010, **282:**1-90.

27. Pope BD, Ryba T, Dileep V, Yue F, Wu W, Denas O, Vera DL, Wang Y, Hansen RS, Canfield TK, et al: **Topologically associating domains are stable units of replication-timing regulation.** *Nature* 2014, **515:**402-405.

28. Oldach P, Nieduszynski CA: **Cohesin-Mediated Genome Architecture Does Not Define DNA Replication Timing Domains.** *Genes (Basel)* 2019, **10**.

29. Sima J, Chakraborty A, Dileep V, Michalski M, Klein KN, Holcomb NP, Turner JL, Paulsen MT, Rivera-Mulia JC, Trevilla-Garcia C, et al: **Identifying cis Elements for Spatiotemporal Control of Mammalian DNA Replication.** *Cell* 2019, **176:**816-830 e818.

30. Cremer M, Grasser F, Lanctot C, Muller S, Neusser M, Zinner R, Solovei I, Cremer T: **Multicolor 3D fluorescence in situ hybridization for imaging interphase chromosomes.** *Methods Mol Biol* 2008, **463:**205-239.

31. Jevtic P, Edens LJ, Vukovic LD, Levy DL: **Sizing and shaping the nucleus: mechanisms and significance.** *Curr Opin Cell Biol* 2014, **28:**16-27.

32. Langer S, Geigl JB, Ehnle S, Gangnus R, Speicher MR: **Live cell catapulting and recultivation does not change the karyotype of HCT116 tumor cells.** *Cancer Genet Cytogenet* 2005, **161:**174-177.

33. Melcher R, Koehler S, Steinlein C, Schmid M, Mueller CR, Luehrs H, Menzel T, Scheppach W, Moerk H, Scheurlen M, et al: **Spectral karyotype analysis of colon cancer cell lines of the tumor suppressor and mutator pathway.** *Cytogenet Genome Res* 2002, **98:**22-28.

34. Schmid VJ, Cremer M, Cremer T: **Quantitative analyses of the 3D nuclear landscape recorded with super-resolved fluorescence microscopy.** *Methods* 2017, **123:**33-46.

35. Lin S, Coutinho-Mansfield G, Wang D, Pandit S, Fu XD: **The splicing factor SC35 has an active role in transcriptional elongation.** *Nat Struct Mol Biol* 2008, **15:**819-826.

36. Spector DL, Lamond AI: **Nuclear speckles.** *Cold Spring Harb Perspect Biol* 2011, **3**.

37. Egloff S, Murphy S: **Cracking the RNA polymerase II CTD code.** *Trends Genet* 2008, **24:**280-288.

38. Zhou VW, Goren A, Bernstein BE: **Charting histone modifications and the functional organization of mammalian genomes.** *Nat Rev Genet* 2011, **12:**7-18.

39. Dimitrova DS, Berezney R: **The spatio-temporal organization of DNA replication sites is identical in primary, immortalized and transformed mammalian cells.** *J Cell Sci* 2002, **115:**4037-4051.

40. Chagin VO, Stear JH, Cardoso MC: **Organization of DNA replication.** *Cold Spring Harb Perspect Biol* 2010, **2:**a000737.

41. Jackson DA, Pombo A: **Replicon clusters are stable units of chromosome structure: evidence that nuclear organization contributes to the efficient activation and propagation of S phase in human cells.** *J Cell Biol* 1998, **140:**1285-1295.

42. Schermelleh L, Solovei I, Zink D, Cremer T: **Two-color fluorescence labeling of early and mid-to-late replicating chromatin in living cells.** *Chromosome Res* 2001, **9:**77-80.

43. Zink D, Bornfleth H, Visser A, Cremer C, Cremer T: **Organization of early and late replicating DNA in human chromosome territories.** *Exp Cell Res* 1999, **247:**176-188.

44. Xiang W, Roberti MJ, Heriche JK, Huet S, Alexander S, Ellenberg J: **Correlative live and super-resolution imaging reveals the dynamic structure of replication domains.** *J Cell Biol* 2018, **217:**1973-1984.

45. Heng HH, Goetze S, Ye CJ, Liu G, Stevens JB, Bremer SW, Wykes SM, Bode J, Krawetz SA: **Chromatin loops are selectively anchored using scaffold/matrix-attachment regions.** *J Cell Sci* 2004, **117:**999-1008.

46. Diaz-Martinez LA, Beauchene NA, Furniss K, Esponda P, Gimenez-Abian JF, Clarke DJ: **Cohesin is needed for bipolar mitosis in human cells.** *Cell Cycle* 2010, **9:**1764-1773.

47. Hintermair C, Voss K, Forne I, Heidemann M, Flatley A, Kremmer E, Imhof A, Eick D: **Specific threonine-4 phosphorylation and function of RNA polymerase II CTD during M phase progression.** *Sci Rep* 2016, **6:**27401.

48. Giebel B, Punzel M: **Lineage development of hematopoietic stem and progenitor cells.** *Biol Chem* 2008, **389:**813-824.

49. Joos S, Granzow M, Holtgreve-Grez H, Siebert R, Harder L, Martin-Subero JI, Wolf J, Adamowicz M, Barth TF, Lichter P, Jauch A: **Hodgkin's lymphoma cell lines are characterized by frequent aberrations on chromosomes 2p and 9p including REL and JAK2.** *Int J Cancer* 2003, **103:**489-495.

50. Takaki T, Montagner M, Serres MP, Le Berre M, Russell M, Collinson L, Szuhai K, Howell M, Boulton SJ, Sahai E, Petronczki M: **Actomyosin drives cancer cell nuclear dysmorphia and threatens genome stability.** *Nat Commun* 2017, **8:**16013.

51. Zwerger M, Ho CY, Lammerding J: **Nuclear mechanics in disease.** *Annu Rev Biomed Eng* 2011, **13:**397-428.

52. Moindrot B, Audit B, Klous P, Baker A, Thermes C, de Laat W, Bouvet P, Mongelard F, Arneodo A: **3D chromatin conformation correlates with replication timing and is conserved in resting cells.** *Nucleic Acids Res* 2012, **40:**9470-9481.

53. Zhao PA, Rivera-Mulia JC, Gilbert DM: **Replication Domains: Genome Compartmentalization into Functional Replication Units.** *Adv Exp Med Biol* 2017, **1042:**229-257.

54. Nakamura H, Morita T, Sato C: **Structural organizations of replicon domains during DNA synthetic phase in the mammalian nucleus.** *Exp Cell Res* 1986, **165:**291-297.

55. Baddeley D, Chagin VO, Schermelleh L, Martin S, Pombo A, Carlton PM, Gahl A, Domaing P, Birk U, Leonhardt H, et al: **Measurement of replication structures at the nanometer scale using super-resolution light microscopy.** *Nucleic Acids Res* 2010, **38:**e8.

56. Marchal C, Sima J, Gilbert DM: **Control of DNA replication timing in the 3D genome.** *Nat Rev Mol Cell Biol* 2019.

57. Hansen AS, Cattoglio C, Darzacq X, Tjian R: **Recent evidence that TADs and chromatin loops are dynamic structures.** *Nucleus* 2018, **9:**20-32.

58. Wang XT, Dong PF, Zhang HY, Peng C: **Structural heterogeneity and functional diversity of topologically associating domains in mammalian genomes.** *Nucleic Acids Res* 2015, **43:**7237-7246.

59. Zhan Y, Mariani L, Barozzi I, Schulz EG, Bluthgen N, Stadler M, Tiana G, Giorgetti L: **Reciprocal insulation analysis of Hi-C data shows that TADs represent a functionally but not structurally privileged scale in the hierarchical folding of chromosomes.** *Genome Res* 2017, **27:**479-490.

60. Rowley MJ, Corces VG: **Organizational principles of 3D genome architecture.** *Nat Rev Genet* 2018, **19:**789-800.

61. Barrington C, Finn R, Hadjur S: **Cohesin biology meets the loop extrusion model.** *Chromosome Res* 2017, **25:**51-60.

62. Fudenberg G, Abdennur N, Imakaev M, Goloborodko A, Mirny LA: **Emerging Evidence of Chromosome Folding by Loop Extrusion.** *Cold Spring Harb Symp Quant Biol* 2017, **82:**45-55.

63. Nuebler J, Fudenberg G, Imakaev M, Abdennur N, Mirny LA: **Chromatin organization by an interplay of loop extrusion and compartmental segregation.** *Proc Natl Acad Sci U S A* 2018, **115:**E6697-E6706.

64. Richterova J, Huraiova B, Gregan J: **Genome Organization: Cohesin on the Move.** *Mol Cell* 2017, **66:**444-445.

65. Naumova N, Imakaev M, Fudenberg G, Zhan Y, Lajoie BR, Mirny LA, Dekker J: **Organization of the mitotic chromosome.** *Science* 2013, **342:**948-953.

66. Gibcus JH, Samejima K, Goloborodko A, Samejima I, Naumova N, Nuebler J, Kanemaki MT, Xie L, Paulson JR, Earnshaw WC, et al: **A pathway for mitotic chromosome formation.** *Science* 2018, **359**.

67. Bernardi G: **Genome Organization and Chromosome Architecture.** *Cold Spring Harb Symp Quant Biol* 2015, **80:**83-91.

68. Jabbari K, Bernardi G: **An Isochore Framework Underlies Chromatin Architecture.** *PLoS One* 2017, **12:**e0168023.

69. Mirny LA, Imakaev M, Abdennur N: **Two major mechanisms of chromosome organization.** *Curr Opin Cell Biol* 2019, **58:**142-152.

70. Sexton T, Yaffe E, Kenigsberg E, Bantignies F, Leblanc B, Hoichman M, Parrinello H, Tanay A, Cavalli G: **Three-dimensional folding and functional organization principles of the Drosophila genome.** *Cell* 2012, **148:**458-472.

71. Bintu B, Mateo LJ, Su JH, Sinnott-Armstrong NA, Parker M, Kinrot S, Yamaya K, Boettiger AN, Zhuang X: **Super-resolution chromatin tracing reveals domains and cooperative interactions in single cells.** *Science* 2018, **362**.

72. Nir G, Farabella I, Perez Estrada C, Ebeling CG, Beliveau BJ, Sasaki HM, Lee SD, Nguyen SC, McCole RB, Chattoraj S, et al: **Walking along chromosomes with super-resolution imaging, contact maps, and integrative modeling.** *PLoS Genet* 2018, **14:**e1007872.

73. Dekker J, Belmont AS, Guttman M, Leshyk VO, Lis JT, Lomvardas S, Mirny LA, O'Shea CC, Park PJ, Ren B, et al: **The 4D nucleome project.** *Nature* 2017, **549:**219-226.

74. Finn EH, Pegoraro G, Brandao HB, Valton AL, Oomen ME, Dekker J, Mirny L, Misteli T: **Extensive Heterogeneity and Intrinsic Variation in Spatial Genome Organization.** *Cell* 2019, **176:**1502-1515 e1510.

75. Krumm A, Duan Z: **Understanding the 3D genome: Emerging impacts on human disease.** *Semin Cell Dev Biol* 2019, **90:**62-77.

76. Szabo Q, Bantignies F, Cavalli G: **Principles of genome folding into topologically associating domains.** *Sci Adv* 2019, **5:**eaaw1668.

77. Otterstrom J, Castells-Garcia A, Vicario C, Gomez-Garcia PA, Cosma MP, Lakadamyali M: **Super-resolution microscopy reveals how histone tail acetylation affects DNA compaction within nucleosomes in vivo.** *Nucleic Acids Res* 2019.

78. Ricci MA, Manzo C, Garcia-Parajo MF, Lakadamyali M, Cosma MP: **Chromatin fibers are formed by heterogeneous groups of nucleosomes in vivo.** *Cell* 2015, **160:**1145-1158.

79. Xu J, Liu Y: **A guide to visualizing the spatial epigenome with super-resolution microscopy.** *FEBS J* 2019.

80. Maeshima K, Kaizu K, Tamura S, Nozaki T, Kokubo T, Takahashi K: **The physical size of transcription factors is key to transcriptional regulation in chromatin domains.** *J Phys Condens Matter* 2015, **27:**064116.

81. Maeshima K, Ide S, Babokhov M: **Dynamic chromatin organization without the 30-nm fiber.** *Curr Opin Cell Biol* 2019, **58:**95-104.

82. Maeshima K, Rogge R, Tamura S, Joti Y, Hikima T, Szerlong H, Krause C, Herman J, Seidel E, DeLuca J, et al: **Nucleosomal arrays self-assemble into supramolecular globular structures lacking 30-nm fibers.** *EMBO J* 2016, **35:**1115-1132.

83. Paulsen J, Liyakat Ali TM, Nekrasov M, Delbarre E, Baudement MO, Kurscheid S, Tremethick D, Collas P: **Long-range interactions between topologically associating domains shape the four-dimensional genome during differentiation.** *Nat Genet* 2019, **51:**835-843.

84. Nmezi B, Xu J, Fu R, Armiger TJ, Rodriguez-Bey G, Powell JS, Ma H, Sullivan M, Tu Y, Chen NY, et al: **Concentric organization of A- and B-type lamins predicts their distinct roles in the spatial organization and stability of the nuclear lamina.** *Proc Natl Acad Sci U S A* 2019.

85. Szczurek A, Klewes L, Xing J, Gourram A, Birk U, Knecht H, Dobrucki JW, Mai S, Cremer C: **Imaging chromatin nanostructure with binding-activated localization microscopy based on DNA structure fluctuations.** *Nucleic Acids Res* 2017, **45:**e56.

86. Lleres D, Bailly AP, Perrin A, Norman DG, Xirodimas DP, Feil R: **Quantitative FLIM-FRET Microscopy to Monitor Nanoscale Chromatin Compaction In Vivo Reveals Structural Roles of Condensin Complexes.** *Cell Rep* 2017, **18:**1791-1803.

87. Lou J, Scipioni L, Wright BK, Bartolec TK, Zhang J, Masamsetti VP, Gaus K, Gratton E, Cesare AJ, Hinde E: **Phasor histone FLIM-FRET microscopy quantifies spatiotemporal rearrangement of chromatin architecture during the DNA damage response.** *Proc Natl Acad Sci U S A* 2019, **116:**7323-7332.

88. Pelicci S, Diaspro A, Lanzano L: **Chromatin nanoscale compaction in live cells visualized by acceptor-to-donor ratio corrected Forster resonance energy transfer between DNA dyes.** *J Biophotonics* 2019:e201900164.

89. Priest DG, Solano A, Lou J, Hinde E: **Fluorescence fluctuation spectroscopy: an invaluable microscopy tool for uncovering the biophysical rules for navigating the nuclear landscape.** *Biochem Soc Trans* 2019, **47:**1117-1129.

90. Markaki Y, Smeets D, Cremer M, Schermelleh L: **Fluorescence in situ hybridization applications for super-resolution 3D structured illumination microscopy.** *Methods Mol Biol* 2013, **950:**43-64.

91. Schermelleh L: **In Vivo DNA replication labeling.** *Cell Biology - a laboratory handbook* 2006, **3rd edition volume 1, editor J.E. Celis, Elsevier Academic Press**

92. Clarke ST, Song Z, Kwan KY, DeMarco C, Rukavishnikov A, Singh U, Gee K: **GFP compatibility with EdU cell proliferation assay.** *DOI: 101158/1538-7445AM2014-5098* 2014.

93. Salic A, Mitchison TJ: **A chemical method for fast and sensitive detection of DNA synthesis in vivo.** *Proc Natl Acad Sci U S A* 2008, **105:**2415-2420.

94. Durand NC, Robinson JT, Shamim MS, Machol I, Mesirov JP, Lander ES, Aiden EL: **Juicebox Provides a Visualization System for Hi-C Contact Maps with Unlimited Zoom.** *Cell Syst* 2016, **3:**99-101.

95. Durand NC, Shamim MS, Machol I, Rao SS, Huntley MH, Lander ES, Aiden EL: **Juicer Provides a One-Click System for Analyzing Loop-Resolution Hi-C Experiments.** *Cell Syst* 2016, **3:**95-98.

96. Javanmoghadam-Kamrani S, Keyomarsi K: **Synchronization of the cell cycle using lovastatin.** *Cell Cycle* 2008, **7:**2434-2440.

97. Marchal C, Sasaki T, Vera D, Wilson K, Sima J, Rivera-Mulia JC, Trevilla-Garcia C, Nogues C, Nafie E, Gilbert DM: **Genome-wide analysis of replication timing by next-generation sequencing with E/L Repli-seq.** *Nat Protoc* 2018, **13:**819-839.

98. Guillou E, Ibarra A, Coulon V, Casado-Vela J, Rico D, Casal I, Schwob E, Losada A, Mendez J: **Cohesin organizes chromatin loops at DNA replication factories.** *Genes Dev* 2010, **24:**2812-2822.

99. Schindelin J, Arganda-Carreras I, Frise E, Kaynig V, Longair M, Pietzsch T, Preibisch S, Rueden C, Saalfeld S, Schmid B, et al: **Fiji: an open-source platform for biological-image analysis.** *Nat Methods* 2012, **9:**676-682.

100. Dobbie IM, King E, Parton RM, Carlton PM, Sedat JW, Swedlow JR, Davis I: **OMX: a new platform for multimodal, multichannel wide-field imaging.** *Cold Spring Harb Protoc* 2011, **2011:**899-909.

101. Pau G, Fuchs F, Sklyar O, Boutros M, Huber W: **EBImage--an R package for image processing with applications to cellular phenotypes.** *Bioinformatics* 2010, **26:**979-981.

102. R Core Team: **R: A language and environment for statistical computing.** In *Book R: A language and environment for statistical computing* (Editor ed.^eds.). City: R Foundation for Statistical Computing, Vienna, Austria; 2013.

Authors contributions

TC and ELA initiated the study; MC and TC conceived the microscopic experiments together with HH; KB, MC and AM performed experiments shown in Figs. 1- 4,6 - 7 and Suppl. Figs. 2- 4. AM and KB performed live cell and super-resolution/confocal microscopy; HH provided input on quantitative image analysis, including statistical analysis; AM performed segmentation analyses and VS 3D image analyses for chromatin density mapping data; SM performed DNA Halo experiments with support of MCC. Hi-C data were generated by SSPR and ELA with experimental support of NM (Fig. 5). Repli-Seq data were provided by DMG and KNK. HL provided input for the 3D imaging part and MCC for the replication part. MC and TC wrote the manuscript with support from all authors, in particular from ELA.

Competing interests

The authors declare to have no competing interests.

Availability of supporting data

All data generated or analyzed during this study are included in this published article and its Additional files.

Consent for publication

All authors read and approved the manuscript.

Ethical approval and consent to participate

Not applicable

Funding